Is Nostoc H-NOX an NO sensor or Redox Switch?

Ah-Lim Tsai[1], **Vladimir Berka**[1], **Faye Martin**[2], **Xiaolei Ma**[2], **Focco van den Akker**[2], **Marian Fabian**[3], and **John S. Olson**[3,#]

[1]Division of Hematology, Internal Medicine, University of Texas Houston Medical School, Houston, TX, USA

[2]Department of Biochemistry, School of Medicine, Case Western Reserve University, Cleveland, OH USA

[3]Department of Biochemistry and Cell Biology, Rice University, Houston, TX. USA

Abstract

Nostoc sp (Ns) H-NOX is a hemeprotein found in symbiotic cyanobacteria, which has ~35% sequence identity and high structural homology to the β subunit of soluble guanylyl cyclase (sGC), suggesting a NO sensing function. However, UV-Vis, EPR, NIR MCD, and ligand binding experiments with ferrous and ferric *Ns* H-NOX indicate significant functional differences between *Ns* H-NOX and sGC. (1) After NO binding to sGC, the proximal histidine dissociates from the heme iron, causing a conformational change that triggers activation of sGC. In contrast, formation of pentacoordinate (5c) NO heme occurs to only a limited extent in *Ns* H-NOX, even at > 1mM NO. (2) Unlike sGC, two different hexacoordinate (6c)-NO complexes are formed in *Ns* H-NOX with initial and final absorbance peaks at 418 nm and 414 nm, and the conversion rate is linearly dependent on [NO] indicating that a second NO binds transiently to catalyze formation of the 414 nm species. (3) sGC is insensitive to oxygen, and ferric sGC prepared by ferricyanide oxidation has a 5c high-spin heme complex. In contrast, *Ns* H-NOX autoxidizes in 24 hr if exposed to air and forms a 6c ferric heme complex indicating a major conformational change after oxidation and coordination by a second histidine side chain. Such a large conformational transition suggests that *Ns* H-NOX could function as either a redox or a NO sensor in the cyanobacterium.

The chemical versatility of heme for reversible coordination of small molecule substrates/activators and redox reactions has been adopted by living cells in all kingdoms for a variety of physiological functions, including gas storage and transport, electron transfer, enzyme catalysis, sensing of diatomic gases, monitoring cellular redox potential, and intra- and intercellular signaling (1–3). With the advance of efficient genomic and proteomic screening in the last decade, increasing numbers of heme proteins involved in O_2, CO, and NO sensing have been identified (4–7). Such signal transduction heme proteins are frequently expressed as two-component systems, usually including one heme-sensor and one transducer (or effector) component, sometimes as domains on the same polypeptide or as separate gene products. Signaling transducer proteins or domains include kinases, phosphodiesterases, chemotaxis machinery and DNA-binding proteins (4,5,8,9).

Corresponding authors: **Ah-Lim Tsai, PhD**, Division of Hematology, Internal Medicine, University of Texas Houston Medical School, MSB 5290, 6431 Fannin, Houston, TX, 77030. Phone: 713 500-6771, fax: 713 500-6810, Ah-lim.tsai@uth.tmc.edu. **Focco van den Akker, Ph.D**, Department of Biochemistry RT500, School of Medicine, Case Western Reserve University, 10900 Euclid Avenue, Cleveland, OH 44106-4935. Phone: (216) 368-8511, fax: (216) 368-3419, fxv5@cwru.edu.

Soluble guanylyl cyclase (sGC) is the major nitric oxide (NO) sensing heme protein for mammals, and its enzyme activity is increased ≥100-fold upon NO binding to the heme containing subunit (10,11). Determination of the exact structural mechanism for the coupling between NO binding to the heme in the β subunit and subsequent activation of cyclase activity in the partner domain remains a challenging problem, in part because there are no crystal structures of either the heme domain or full-length mammalian sGC. However, structural and mechanistic studies of homologous proteins can provide useful insights into the activation mechanism of human sGC and other sensors in response to NO. Genomic screening has identified several microbial heme protein sensor domains, called H-NOX (Heme-Nitric oxide and OXygen binding) or SONO (Sensor Of NO), that have significant sequence identity with the human sGC β subunit and are potential model systems for studying the kinetics and structural changes associated with ligand binding to the heme domain of sGC (8,12,13). The crystal structures of sensor proteins from *Thermoanaerobacter tengcongensis* (*Tt* H-NOX) and *Nostoc sp* (*Ns* H-NOX) have been determined and provided mechanistic insights into the reactions of sGC with NO (12–14). *Ns* H-NOX appears to be a better sGC model than *Tt* H-NOX because of its higher sequence identity (33% vs. 18%) and similar apparent *in vivo* function (12,14). The *Tt* H-NOX domain appears to be an oxygen sensor, whereas *Ns* H-NOX, like sGC, does not appear to bind O_2 directly but is capable of binding both NO and CO. The key residues responsible for ligand discrimination by sGC and homologues have been shown to locate primarily in the distal heme-binding pocket and are significantly closer in identity between *Ns* H-NOX and sGC than for any other bacterial homolog (12).

We have examined in detail the kinetics of NO, CO, and O_2 binding to *Ns* H-NOX using a variety of spectroscopic, rapid mixing and flash photolysis methods to determine the functional similarity of this bacterial protein to sGC. *Ns* H-NOX is capable of binding NO and CO rapidly, but the binding mechanisms, particularly for NO, show differences from those observed for sGC. Most significantly *Ns* H-NOX forms a predominantly 6-c NO heme complex whereas sGC immediately forms the 5-c state resulting from cleavage of the proximal histidine, which is required for activation of the catalytic domain. The heme group in *Ns* H-NOX autooxidizes, albeit slowly over hours, whereas sGC is insensitive to oxygen for days at a time. The latter *in vitro* observation contrasts with long-standing evidence that sGC undergoes oxidation *in vivo* during certain disease states (15,16). Oxidation of sGC results in loss of activity and proteosomal degradation, however, recent heme-independent activators that target oxidized sGC have been shown to restore sGC activity *in vivo* (17). These observations warrant a reexamination of redox regulation of sGC and H-NOX enzymatic activity previously deemed an artifact.

Our results explore and attempt to explain the differences between sGC and *Ns* H-NOX, shed light on the function of *Ns* H-NOX, and extend the context in which we not only can explore sGC function but also new functions in a wider scope. In agreement with and analogous to the wide range of roles played by heme protein-sensors, it is likely that, in addition to sensing NO, *Ns* H-NOX also monitors the general redox potential of the bacterium's environment.

Material and Methods

Materials

Carbon monoxide and nitric oxide gas were from Matheson-TriGas and nitrous and nitric acid was removed from the latter by passing the gas through a NaOH trap. Potassium ferricyanide, sodium hydrosulfite (~85%), sodium nitrite (97%), sodium azide, potassium cyanide, imidazole, bovine heart cytochrome c, deuterium water, dithiothreitol (DTT), β-mercaptoethanol (β-BME), isopropyl-1-thio-β-D-galactopyranoside (IPTG), δ-

Aminolevulinic acid, phenylmethyl-sulfonyl fluoride (PMSF), glycerol, EDTA were purchased from Sigma-Aldrich. Bicinchoninic acid reagents (BCA reagents) are from CalBiochem. 1M cyanide solution, ~pH 9, was prepared by titration of potassium cyanide by 6N HCl at 0 °C on ice. Other chemicals are all reagent grade.

Protein expression and purification

Ns H-NOX 1–183 in pET22b was expressed in Rosetta DE3 pLysS cells (Novagen). Freshly transformed colonies were grown to an OD of 0.4–0.5 in Terrific Broth with appropriate antibiotics at 37°C. Growth temperature was adjusted to 30 °C and cultures were induced by addition of IPTG to 20 µM and δ-Aminolevulinic acid to 2 mM followed by incubation overnight. Cells were harvested by centrifugation at $5000 \times g$. Pellets were resuspended in 50 mM NaCl H-NOX Buffer (20 mM TRIS, 5 mM β-BME, 2 mM PMSF) and the suspensions were flash frozen in liquid nitrogen and stored at −80 °C.

Cells were thawed and frozen 3 times; solid DTT was added to 100 mM; the suspension was sonicated until homogenous; and the final sample centrifuged at $20,000 \times g$ for 20 min at 4°C. *Ns* H-NOX protein was purified as described previously (14). The cleared H-NOX lysate was purified sequentially over 1) Hi-trap, 2) Superdex 200, 3) Mono Q, 4) Superdex 75 columns[11]. Peak fractions with A_{420}/A_{280} ratio greater than 2.0 were pooled and concentrated. Protein concentration was determined by bicinchoninic acid, or BCA method (18), using 1 mg/ml human serum albumin as standard.

Pyridine hemochromogen assay

Heme content was determined by the formation of pyridine hemochromogen as previously described (19). In brief, the spectrum of ~ 100 µg isolated fresh ferrous *Ns* H-NOX or oxidized sample containing 0.15 M NaOH, 1.8 M pyridine was recorded and then few grains of solid dithionite were added. The total heme content was determined from the reduced minus oxidized difference spectrum of bis-pyridine heme using $\Delta A_{556-538}$ nm = 24 mM^{-1} cm^{-1}. A metmyoglobin standard (A_{409} = 157 mM^{-1}cm^{-1}) was run in parallel as a control.

Determination of binding equilibrium constant by optical titration

Equilibrium dissociation constants were estimated as the ligand concentration at the half maximal absorbance in titration experiments which monitored the fractional absorbance difference between the initial ligand free *Ns* H-NOX and the sensor fully saturated by the ligand. The binding isotherm between delta absorbance and ligand concentration constructed by optical titration with serial additions of the ligand were fit to a single-binding site hyperbolic function: $\Delta A_i = \Delta A_{max} [L]_i / (K_d + [L]_i)$, where ΔA_i is the absorbance difference after the ith addition of ligand, ΔA_{max} is the maximal absorbance change when the protein was saturated with ligand, K_d is the equilibrium dissociation constant, and $[L]_i$ is the free ligand concentration after the ith addition. Volume changes due to ligand addition were corrected for and were no more than 5%. All titrations were conducted in 50 mM HEPES, pH 7.7 containing 10% glycerol and 0.1 M NaCl.

Stopped-flow experiments

In most cases association and dissociation rate constants, k_{on} and k_{off}, respectively, were determined using rapid mixing measurements in an Applied Photophysics model SX-18MV stopped-flow instrument with a rapid-scan diode-array accessory (20). Kinetic measurements were normally conducted under pseudo first-order conditions with ligand concentration at least an order of magnitude greater than that of the protein. Ligand binding to the ferric sensor was done aerobically at 1:1 (V/V) equal mixing. For anaerobic experiments with NO and CO binding, the fluid channels in the stopped-flow apparatus were

incubated with a dithionite solutions for several hours and then rinsed with nitrogen-saturated buffer. Reactants were rendered anaerobic by 5 cycles of vacuum/argon replacement in a tonometer. The reaction time courses were analyzed by nonlinear regression to single or multiple exponential functions. Estimated k_{on} and k_{off} values were derived from the slope and y-intercept, respectively, in plots of k_{obs} versus ligand concentrations.

Laser flow-flash kinetic measurements

The kinetics of NO binding to *Ns* H-NOX were measured by flow-flash methods as described previously by Salter et al. in studies with *Cerebratulus lacteus* hemoglobin (Hb) (21). An anaerobic solution of reduced protein in complex with carbon monoxide (0.1 mM CO) was rapidly mixed at 1:1 ratio with a buffer containing 2 mM NO. Then, ~50 ms after flow stopped, the CO complex of the *Ns* H-NOX was photolyzed by a 0.5 µs excitation laser pulse at 577 nm (phase-R 2100 dye laser). The kinetics of NO association to the reduced protein was monitored at 436 nm and 20 °C. Rapid mixing of solutions was controlled by a Bio-Logic stopped-flow module SFM 400 (Molecular Kinetics, Inc. Indianapolis, IN).

EPR spectrometry

EPR spectra were recorded at liquid helium or liquid nitrogen temperatures on a Bruker EMX spectrometer (22). Data analysis and spectral simulations were conducted using WinEPR and SimFonia programs furnished with the EMX system. The conditions for liquid nitrogen EPR measurements were: frequency, 9.29 GHz; modulation amplitude, 2 G; modulation frequency, 100 kHz; and time constant, 0.33 s. Liquid helium EPR conditions were the same, except with frequency, 9.61 GHz; and modulation amplitude, 2 or 10 G. The microwave power dependence was fit by nonlinear regression to the equation: $\log (S/P^{1/2}) = -b/2 \log (P^{1/2} + P) + b/2 \log(P^{1/2}) + \log K$, where P is the power, S is the peak to trough amplitude of the EPR signal, $P^{1/2}$ is the power at half-saturation, and b and K are floating parameters with $b = 1$ for non-homogeneous saturation (23).

Near infrared magnetic circular dichroism (NIR MCD)

MCD spectra between 800 and 2000 nm were acquired in a JASCO J730 using a 150 W tungsten-halogen lamp and a liquid nitrogen cooled high sensitivity InSb detector equipped with a 1.4 T electromagnet. CD wavelength and sensitivity was calibrated by 1:1 mixture of 0.24 M $NiSO_4$ and 0.36 M K^+,Na^+−d-tartrate. All measurements were performed at room temperature (24 °C) at a bandwidth of 10 nm, 1 s time constant, 0.5 nm step resolution from 2000 to 800 nm at 200 nm/min scan speed. MCD calculation from H^+ (CD + MCD) and H^- (CD − MCD) and adjusted for molar delta absorption coefficient: $\Delta A(M \, cm \, T)^{-1}$ was done by the Spectral Analysis software that came with the J730 system provided by JASCO.

Far-UV CD

CD spectra between 190 to 290 nm were recorded in a JASCO J815 using a 150 W xenon lamp. All measurements were performed at room temperature (24 °C) at a spectral bandwidth of 1 nm, 0.5 s time constant, 0.2 nm step resolution at 200 nm/min scan speed. 12 repetitive scans with 2 mm path quartz cuvette were recorded for each protein sample as well as the buffer control.

Results

Heme and protein quantitation

Total heme concentration of isolated *Ns* H-NOX protein was quantified by pyridine hemochrome assay. A fresh ferrous *Ns* H-NOX sample yielded a molar absorbance

coefficient of 170 mM^{-1}cm^{-1} at 429 nm. The molar absorption coefficient for the ferric Soret peak at 414 nm was determined to be 136 mM^{-1}cm^{-1}. Protein concentration determined by the BCA method and combined with the pyridine hemochromogen assay gave a heme stoichiometry of 1.05 ± 0.13 (n = 3) per protein monomer. The ratio of the 414/280 nm for Fe(III) *Ns* H-NOX is 2:1 and the ratio of 429/280 for the ferrous form is 3:1. The purified protein appears to be > 90% homogeneous based on SDS PAGE analysis and Superdex 75 chromatographic analysis.

Autooxidation of Ns H-NOX

Heterodimeric full length sGC is relatively insensitive to autooxidation in the presence of air or 1 atm oxygen (24). When we placed an aerobic solution of the *Ns* H-NOX sensor, which had been stored aerobically in 5 mM DTT, in a tonometer and purged the gas space with argon, there was a ~3 nm red-shift of the Soret peak from 426 to 429 nm, suggesting that the original sample was partially oxidized and then was re-reduced anaerobically with DTT. To examine autooxidation more directly, a reduced preparation of *Ns* H-NOX with a 429 nm Soret peak was gel filtered to remove all DTT from the storage buffer, and then monitored for oxidation by recording its optical spectral at 24 °C over a period of two days. A Soret band shift from 429 nm to 414 nm occurs slowly with a discrete isosbestic point at 419 nm, indicating conversion from Fe(II) to Fe(III) with autooxidation at a rate ≈ 0.05 h^{-1}. This value is similar to the rate of autooxidation of oxymyoglobin (MbO$_2$) and about 4-fold greater than that for human oxyhemoglobin (HbO$_2$) (25,26) (Fig. 1). Thus the *Ns* H-NOX heme iron is capable of donating electrons to O$_2$, albeit very slowly. However, there is no observable Fe(II)O$_2$ intermediate during this process, suggesting that the affinity of *Ns* H-NOX for O$_2$ must be very poor, i.e. P$_{50} \gg 1000$ μM, presumably due to a very large dissociation rate constant.

Spectroscopic and kinetic characterization of CO binding

We characterized CO and NO binding to *Ns* H-NOX for direct comparison with the ligand binding properties of sGC (27–29). CO binding to ferrous *Ns* H-NOX shifts the Soret peak from 429 nm to 422–423 nm (14) and is a simple one-step reaction with no spectral intermediates when examined by rapid scanning, stopped-flow spectrophotometry. Time courses at 420 nm were measured under pseudo first-order reaction conditions using 5 μM ferrous *Ns* H-NOX and varying [CO] from 25 to 166 μM at 24 °C (Fig. 2a). Observed rates were obtained by fitting to one-exponential expressions, and k$_{obs}$ depends linearly on [CO], with a calculated second-order rate constant = $2 - 3 \times 10^6$ M^{-1}s^{-1} based on data for two separately expressed and purified *Ns* H-NOX samples (Fig. 2a, Inset). The total absorbance changes obtained with seven different CO concentrations were the same indicating that complete saturation with ligand was achieved and that the K$_d$ for CO binding is < 25 μM. The y-axis intercept of the k$_{obs}$ versus [CO] gave an unusually high value of 23 s^{-1} for the CO dissociation rate constant (k$_{off}$), which when combined with an association rate constant of 2.9 μM^{-1}s^{-1}, gives an estimated K$_d$ for CO binding of $\le$ ~8 μM.

We attempted to measure the CO dissociation rate constant more directly by mixing the CO form with excess NO, which is normally the best method to measure k$_{off}$ for the CO complexes of hemeproteins. When the CO complex of *Ns* H-NOX is mixed with 1 mM NO in the stopped-flow diode-array spectrophotometer (Fig. 2b), a moderately rapid decrease in absorbance at 422 nm occurs and is accompanied by a blue shift of the Soret peak to 418 nm, indicative of displacement of CO and formation of a six coordinate NO complex. On longer time scales, additional absorbance decreases at both 422 and 418 nm, and a further blue shift of the NO-heme peak to 414 nm are observed. Thus, the absorbance decrease at 422 nm is biphasic. The large (80%) initial phase occurs with a first order rate of 3.6 s^{-1}, which is independent of [NO]. Surprisingly, the rate of the second, slower phase shows a

linear dependence on [NO]. Similar rates and dependences on [NO] were obtained from global analysis of complete sets of spectra from the diode array system (not shown), and all of these data are similar to the slow phases observed for excess NO binding to the reduced protein (Fig. 3).

The initial dominant phase for the NO displacement reaction is first order and represents the conversion from Fe(II)CO to the 6c Fe(II)NO complex (418 nm). The secondary slower and smaller phases appears to represent interconversion of a 6c NO bound H-NOX with a peak at 418 to another 6-c NO complex with a peak at 414 nm and a small amount of 5c-NO complex, as indicated by the shoulder at 399 nm in the final spectrum (Fig. 2b). Regardless of the interpretation of the slow phase, the fast phase provides a direct measure of CO dissociation with $k_{off} = 3.6$ s^{-1}. Re-binding of excess CO to these altered NO complexes is unlikely because the overall equilibrium affinity of *Ns* H-NOX for NO is 4 orders of magnitude greater than that of CO (Table 1). The estimated CO dissociation rate from the fast NO displacement phase, $k_{off} = 3.6$ s^{-1}, can be used as the Y-intercept in the linear fit for plots of k_{obs} versus [CO] in the simple CO binding data shown in Fig. 2a, inset, and the resultant slope gives an association rate constant for CO binding, k_{on}, equal to 3.0 µM^{-1}s^{-1}. The ratio of these values, 3.6 s^{-1}/3.0 µM^{-1}s^{-1} provides an estimate of 1.2 µM for the K_d for CO binding to *Ns* H-NOX, which is compatible with equilibrium titration data and previous measurements for H-NOX proteins.

Characterization of NO binding mechanism

NO binding to *Ns* H-NOX heme was studied using rapid mixing stopped-flow and flow-flash laser photolysis approaches to examine all time scales. Rapid-scan diode array measurements of NO binding to Fe(II) *Ns* H-NOX were conducted at low [NO] using either 1:1 protein:NO mixtures or a 5-fold excess of ligand. When only a stoichiometric amount of NO is present, the reaction shows a single rapid phase, with a Soret peak shift from 429 nm to 418 nm and an isosbestic point at 422 nm. Most of the reaction, > 90%, was lost in the 1.5-ms dead-time of the stopped-flow apparatus (Fig. 3a, top). At a 5-fold excess of NO, the initial rapid phase is complete in the dead time, and a second slower phase occurs on milliseconds to second time scales, involving a blue shift in the Soret band from 418 nm to 414 nm. Eventually, two bands form at 414 and 399 nm on seconds to minute time scales and the 399 nm band indicates formation of significant amount of a 5c NO-heme complex (Fig. 3a, bottom). Most of these secondary absorbance changes appear to represent a transition from one 6c-NO complex with a "normal" peak at 418 nm to a second 6c-NO complex with a peak at 414 nm. The rate of decay of the initial 6c-NO complex to the species with a peak at 414 nm depends linearly on [NO] (Fig. 3b, inset), with a slope equal to ~2.0 µM^{-1}s^{-1} and a y-intercept close to 0. The rate-limiting step for this interconversion of 6c NO-heme complexes appears to require transient binding of a second NO molecule.

This second transition is followed by a third process, which is first order and involves a slow biphasic conversion of the 6c-NO complexes to 5c-NO complexes, with first order rate constants equal to ~7 and 0.3 s^{-1}, respectively (Fig. 3b). Only ~40% conversion to a 5c-NO complex with a peak at 399 nm is observed even at [NO] ≈ 1000 µM, and the rate of conversion to the 5c species does not appear to depend on [NO] (Fig. 3b, longer time scale).

In order to determine the association rate constant for the formation of the first 6c-NO complex accurately, we performed flow flash experiments. The CO form of ferrous *Ns* H-NOX was rapidly mixed with NO then photolyzed with a 0.5 µs laser pulse at 577 nm to generate transiently the unliganded ferrous form of *Ns* H-NOX. The binding of NO to unliganded H-NOX was then monitored at 436 and 418 nm under pseudo first-order conditions (i.e. [NO]≫[heme]). The dependence of the observed rates for these ultrafast phases on [NO] gave an association rate constant equal to 200 – 400 µM^{-1}s^{-1}, at 24 °C

(Fig. 4a), which indicates an open, highly accessible active site. Thus, the initial NO binding step is very rapid and almost diffusion controlled, but in the presence of excess NO this species is relatively short-lived and decays to a second 6c NO complex with a peak at 414 nm.

Because the second *Ns* H-NOX 6c-NO complex appears to require additional NO, we attempted to generate only the first 6c-NO complex with a Soret peak at 418 nm by adding a slightly higher than stoichiometric amount of NO anaerobically and then measuring the rate of NO dissociation from this initial complex by mixing it with 0.5 mM CO containing 25 mM dithionite as an NO scavenger. The high concentration of dithionite scavenges any free NO preventing its rebinding, and the rate limiting step for the formation of the CO complex is the initial rate of NO dissociation from the 6c complex. The formation of the CO complex was measured at 423 nm and indicated displacement of bound NO (Fig. 4b). Time courses measured at either 423 or 400 nm were biphasic and gave similar first order rate constants, 0.05 and 0.007 s^{-1}, respectively for the prominent fast and minor slow phases. Assuming that $k_{off} \approx 0.05$ s^{-1} and $k_{on} \approx 300$ µM^{-1}s^{-1} apply for the formation of the initial 6c-NO complex, the apparent K_d for first NO binding step would be ~0.17 nM, which is roughly 100-fold higher than the K_d for NO binding to most mammalian Hbs and Mbs (30).

EPR characterization of resting Ns H-NOX and its complex with NO

The EPR spectrum of the purified H-NOX in the presence of DTT is shown in Fig. 5. The sensor as isolated is mostly ferrous, but some oxidized high and low-spin heme signals are visible at ~ g=6 and ~2.3, respectively, together with some nonspecific iron signals at g= 4.3. The ferric signals are probably a consequence of slow oxidation during storage in air, even in the presence of DTT. During autooxidation in air, the two heme signals increase substantially with more than half the integrated intensity coming from the low-spin Fe(III) form. The high-spin signal around g=6 is heterogeneous and has both rhombic and axial components. The low-spin heme signals at g=3.00 and 2.26 are more visible, and the third g component predicted to be at g=1.37 is not quite visible because it is very broad (31). Further treatment of H-NOX by ferricyanide to oxidize the sensor completely increases the amplitudes but does not change the relative amounts of the high and low spin components. The proportion of the high-spin to low-spin heme in the ferric *Ns* H-NOX changes from batch to batch of purified protein with the low-spin species dominating and in some cases accounts for essentially 100 percent of the sensor as estimated by the MCD signal amplitude of the Soret band and ligand-to-metal charge-transfer band around 600 nm (Tsai et al., unpublished results) (32). Addition of excess imidazole (50 mM) to the ferric sensor abolished the high-spin heme signals and led to a homogeneous low-spin 6c bis-imidazole heme complexes with three principal g values at 2.94, 2.31 and 1.42 (Fig. 5).

When 80 µM ferrous *Ns* H-NOX was mixed with a stoichiometric amount of NO, only a low-spin NO-heme complex EPR was observed in the g = 2 region, without any other observable paramagnetic species (Fig. 5, bottom spectrum). The reduced NO-heme spectrum is dominated by a 6c low-spin signal with 3×3 hyperfine/super hyperfine features contributed by the two axial nitrogen nuclei, one from the N atom of bound nitric oxide and the other from the Nε atom of the proximal histidine (Fig. 6, bottom solid spectrum). The EPR spectrum can be simulated by two nitrogen nuclei with 24 G isotropic hyperfine (nitric oxide N), 6 G isotropic super hyperfine splitting (histidine Nε), a three principal g values of 2.080, 1.975 and 2.003 for g_x, g_y and g_z, respectively, and an additional $g_{y'}$ component (Fig. 6, bottom dached spectrum). The optimal hyperfine splittings for the g_y and g_x obtained by simulation are 10 and 12 Gauss, respectively. The intrinsic line width of the g_y component is relatively large in comparison to the other two g components. This 6c NO heme complex forms very rapidly at ratios of heme to NO of 1:1 (data not shown) and 2:1 and is stable for extended periods of time under anaerobic conditions.

The spectrum for the 1:1 the wild type *Ns* H-NOX NO-heme complex acquired at 10K has better resolution in the hyperfine and super hyperfine feature than that acquired at 110K but otherwise is very similar and typical for a 6c-NO/histidine heme complex. A microwave power dependence study conducted at 110K yielded a half saturation power > 100 mW if the data are treated as homogeneous broadening for a powdered sample (Fig. 6, Inset). This result indicates the presence of a fast energy relaxation mechanism. The spectrum acquired at 4 mW was used for spin quantification against a 1mM $CuSO_4$ and indicated that the amount of NO complex formed at 1:1 or 1:2 ratio is ≥ 90% of the expected amount of spin based on the protein concentration.

When a large excess (1 atm) of NO gas is added directly delivered to an anaerobic wild type *Ns* H-NOX sample, the final NO-heme complex is ~ 40% 5c NO-heme based on the amount of 3-line hyperfine spectra that is present in the EPR spectrum. This observation corroborates earlier electronic spectral data (14) and our interpretation of the initial and final species in our optical stopped-flow data for the reaction of NO with reduced H-NOX (Fig. 3a).

Identification of axial ligands in oxidized H-NOX

The "truth diagram analysis" developed by Blumberg and Peisach (33) is useful for determining the potential axial heme ligands for the low-spin ferric heme H-NOX complexes by examining the correlation between heme rhombicity and the distal ligand tetragonal field strength. Analysis of the native low-spin ferric heme and imidazole derivative signals of H-NOX indicates that the native oxidized sensor has both proximal and distal imidazole ligands because the correlations between rhombicity and field strength are located in the B zone of the Truth Diagram (Fig. 7, grey circles) (23).

This conclusion seems supported by the almost super-imposable optical spectra of oxidized *Ns* H-NOX and its imidazole complex (data not shown). Both have a Soret peak at 414 nm. However, there is no distal histidine side chain located near the heme iron atom in the crystal structure of ferrous *Ns* H-NOX. The closest distal histidine, His150, has its Nε 17.6 Å from the heme iron (14). The correlations in the Truth diagram analysis show that the oxidized *Ns* H-NOX sensor also falls in the center of the narrower "C" zone, which overlaps that for the "B" or bis-His region. The "C" zone is for hemeproteins with methionine/histidine ligand pairs, which are commonly found in c type hemeproteins. There are two methionine residues, Met1 and Met144 (Fig. 8) within 8 Å distance from the heme in the distal portion of the heme pocket of ferrous *Ns* H-NOX (PDB identifier 2O09). The orientation of Met144 seems more favorable than Met1 for coordination of the heme iron but is still ~7.6 Å from the heme iron. However, M144I H-NOX EPR and NIR MCD spectra are almost identical to those of the wild type sensor, excluding M144 as the axial ligand in the ferric H-NOX (Figs. 9 and 10). Thus, regardless of the exact interpretation of the Truth Diagram EPR analysis, there must be a substantial protein conformational change that enables a direct coordination of either His150 or the sulfur atom of Met1 to the heme iron after oxidation. The hypothesis of Met-heme-His coordination is supported by the similar rhombic low-spin EPR signal of ferric cytochrome c, which has Met/His ligand pair (Fig. 9). In addition to the low-spin heme signals, the ferric *Ns* H-NOX sample also has significant amounts of rhombic high-spin heme at g=6 and some non-specific iron at g= 4.3, just as that seen in Fig. 5. In contrast, the imidazole ferric *Ns* H-NOX complex shows a homogeneous low-spin species, indicating that the heterogeneous EPR spectrum of the ferric *Ns* H-NOX probably originates from the difference of distal ligand field strength between imidazole and methionine and resulted in a mixture of 5c-heme-His and 6c His-heme-His or Met-heme-His species.

Near Infrared MCD (NIR MCD)

The ligand to metal charge-transfer (LMCT) MCD signal in the near IR region of the low-spin ferric hemeproteins is another useful diagnostic tool for axial ligand identity. This method complements EPR spectrometry and often enables unambiguous assignment of heme ligands for low-spin ferric heme complexes (34). Met-His ligand pairs have unique NIR MCD signals in the 1700–1900 nm region, whereas the His-His ligand pairs show a signal in the 1450–1600 nm range. A ~65 µM oxidized *Ns* H-NOX sample prepared in D_2O buffer was used for NIR MCD measurement in parallel with ~500 µM cytochrome c, containing an authentic Met/His ligand pair (Fig. 10).

The peak of cyt c is at 1732 nm, corresponding to Met/His heme ligation, as previously published (34). The peak of *Ns* H-NOX MCD is at 1584 nm. There are several possible ligand combinations for this charge-transfer energy range including His/His, His/Lys, and His⁻/Met pairs (34). The His-Lys pair is not supported by the EPR data. The g values observed for the typical model hemeproteins containing His/Lys ligand pairs fall into the "CN⁻" zone of the Truth Diagram (Fig. 7)(35,36). In addition, the closest lysine residue in *Ns* H-NOX, Lys7, is >15 Å from the heme iron (14). As with the ε-amino N atom of Lys, the α-amino group of Met1 cannot be an axial ligand candidate either because of the expected position of its g-values in the "H" region of the EPR "Truth Diagram" (37). The His⁻-Met combination is supported by the NIR MCD data, but the location of low-spin heme with such a ligand pair in the Truth Diagram is predicted to be in the "H" zone due to the additional charge on the histidine (37). The possibility of having the pyrrole N atom of the indole side chain of W74 as axial ligand is not high even though this atom is located only 4Å away from the iron atom. There are no existing examples of a model heme or hemeprotein complex with an indole N atom as an axial ligand, presumably due to steric hindrance of the C_z atom of the benzene ring as well as the high pK_a of the indole proton. Thus, the only axial ligand combination of the *Ns* H-NOX low-spin ferric complex which satisfies both the EPR and NIR MCD characterizations is a His/His pair.

Protein secondary structure changes with heme redox state transition

If coordination by a distal histidine side chain occurs in the ferric state, then oxidation of H-NOX must induce a significant conformational change to bring His150 or another histidine side chain into the active site. To examine this possibility, we recorded Far-UV CD spectra for the ferric and ferrous forms of unliganded *Ns* H-NOX. As shown in Fig. 11, both reduced and oxidized sensors have well defined α helical secondary structure. The ferric *versus* ferrous CD difference spectrum shows a peak at 218, a trough at 196 nm, and a zero crossover at 207 nm, indicating a loss of α-helix structure upon oxidation that could allow bis-histidyl coordination of the heme iron.

Characterization of cyanide and azide binding to ferric Ns H-NOX

Optical titration of ~3 µM ferric *Ns* H-NOX with cyanide showed a simple hyperbolic binding isotherm. The Soret peak shifts from 414 nm to 418 nm and the maximal change occurs at 406 nm. The dissociation constant, K_d, for cyanide binding obtained by non-linear fitting to Eq. 1 is 0.65 mM at 24 °C (Fig. 12A, black circles). A similar titration with azide yielded an apparent K_d of 0.54 mM (Fig. 12A, red circles). Both of these values are large compared to Hbs and Mbs indicating significant hindrance to binding, presumably because of the need to displace one of the bis-histidyl ligands.

Time courses for azide binding to ferric *Ns* H-NOX were examined by stopped-flow absorbance measurements under pseudo first order conditions. The observed rate constants were roughly independent of $[N_3^-]$ in the range from 31.2 to 250 mM and equal to ~ 0.015 s^{-1}. These results indicate that the rate-limiting step for azide binding is first order

dissociation of one of the endogenous axial ligands in the low-spin ferric complex (Fig. 12B, red circles). Cyanide binding kinetics are biphasic with a fast phase accounting for ~40% of the total absorbance changes. The fast phase shows a clear hyperbolic dependence on [CN$^-$], whereas the slow phase shows little dependence on ligand concentration and exhibits a first order limiting rate ≈ 0.13 s^{-1} (Fig. 12B, blue circles). The observed rate for the fast phase of cyanide limited off to a value of 1.8 s^{-1} at [CN$^-$] $\geq$ 100 mM. For both phases, a first order process limits cyanide binding and presumably represents dissociation of one of the endogenous ferric axial ligands. The two phases for cyanide binding could reflect the heterogeneity seen in the EPR signals, which is not manifest for the more slowly reacting azide ligand or it could reflect a more complex reaction mechanism involving a *bis*-cyanide intermediate. However, the key observation is that both azide and cyanide binding are limited by dissociation of one of the internal bis-axial ligands in ferric H-NOX.

Discussion

Comparisons between the ligand binding properties of sGC and Ns H-NOX

Despite significant sequence homology in the distal heme pocket between sGC β subunit and the *Ns* H-NOX (12,14), our current study has revealed six significant differences between the ligand binding properties of these two heme proteins, which may indicate an alternative physiological function for *Ns* H-NOX.

(1) *Ns* H-NOX forms a relatively stable 6c-NO complex at 1:1 and 1:2 heme:NO ratios. A 5c-NO complex is formed at very high [NO], as was measured earlier, but the extent is $\leq$ 40% (14). In contrast, when one equivalent of NO is mixed with sGC, a transient 6c-NO complex is formed, but isomerizes rapidly and completely to the final equilibrium form of the enzyme, which is a 5c NO-heme complex with a Soret peak at 399 nm and a classical three-line EPR spectrum indicating only one axial N atom (38). In the presence of one equivalent of NO, *Ns* H-NOX only forms a 6c-NO complex with a peak at 418 nm and a nine line EPR spectrum indicating two axial N atoms bound to the reduced iron (Figs 3–6). Very high concentrations of NO are required to convert some of the reduced *Ns* H-NOX to a 5c NO complex.

(2) Two different 6c-NO complexes are observed when *Ns* H-NOX is mixed with excess NO. The first species has the same spectral characteristics (i.e. Soret peak at 418 nm) as the initial transient hexacoordinate NO-heme-His complex observed for sGC and is formed very rapidly (k'$_{on}$ $\approx$ 300 µM^{-1}s^{-1}) in a simple bimolecular association reaction. The second *Ns* H-NOX species is unique, with a peak at 414 nm but a typical nine line NO-heme-His EPR spectrum. Unexpectedly, the rate of formation of this second, 6c species exhibits a linear dependence on [NO]. It seems likely that a transient bis-NO-heme intermediate is involved in the formation of the second 6c-NO complex. This transition probably involves a significant conformational change, perhaps mimicking that required for the binding of the second axial protein ligand to the oxidized H-NOX. One possible mechanism is: where **ON-heme-N*** represents the 414 nm species with the altered conformation with either an altered His105 conformation or the second axial ligand with an N atom, i.e. the His150 imidazole base. Applying steady-state assumptions for the pentacoordinate NO-heme and bis-NO-heme complexes, the observed rate for this second phase is:

$$k_{secondary}(obs) = \frac{k_{-His}k'_{NO,2}[NO]k_{N*-NO}}{k_{+His}k_{-NO,2} + k_{+His}k_{N*-NO} + k'_{NO,2}[NO]k_{N*-NO}}$$

Equation 1

At low [NO], the $k'_{NO,2}[NO]k_{N*-NO}$ term in the denominator can be neglected, the observed rate of the slow phase is predicted to be linearly dependent on [NO]

$$k_{secondary}(obs)=k'_{NO,2}[NO]K_{-His}\frac{k_{N*-NO}}{(k_{-NO,2}+k_{N*-NO})}$$

<div align="right">Equation 2</div>

Thus, the apparent second order rate constant is determined by the product of the equilibrium constant for proximal histidine dissociation from the initial 6c complex (K_{-His}), the bimolecular rate constant for the binding of the second NO, $k'_{NO,2}$, and the fraction of bis-NO-heme complexes that either lose the second NO or re-react with a protein histidine side chain to make a more stable complex, (i.e., $k_{N*-NO}/(k_{N*-NO} + k_{NO,2})$). This mechanism rationalizes the linear dependence of the rate of the second phase on [NO] with a y-intercept ≈ 0 (Fig. 3b) and explains why the 418 nm to 414 nm spectral transition only occurs in the presence of excess NO.

(3) Conversion of the *Ns* H-NOX 6c-NO complex to a 5c-NO complex is a slow biphasic process, not dependent on [NO] and is only partially complete ($\leq 40\%$). In contrast, conversion from the initial 6c NO-heme-His complex to a 5c NO-heme species occurs rapidly and completely for sGC, even at 1:1 NO to protein (Martin, E., Berka, V. and Tsai, A.-L., unpublished data). In addition, the 6c to 5c conversion depends linearly on [NO] for sGC (28,38), implying a mechanism similar to that in Scheme I for the formation of the final 6c His-heme-NO complex of *Ns* H-NOX. A possible mechanism for formation of 5c NO-heme in sGC is: **Heme-NO*** represents the altered and activated 5c conformation of the enzyme, perhaps with NO on the proximal side of heme. Again, the second NO is acting catalytically to facilitate formation of the new 5 coordinate complex, and the observed rate for formation of pentacoordinate sGC is also predicted to depend on [NO] as shown below and observed experimentally (27,28)

$$k_{5c}(obs)=\frac{k_{-His}k'_{NO,2}[NO]k_{-NO*}}{k_{+His}k_{-NO,2}+k_{+His}k_{-NO*}+k'_{NO,2}[NO]k_{-NO*}} \approx k'_{NO,2}[NO]K_{-His}\left(\frac{k_{-NO*}}{k_{-NO,2}+k_{-NO*}}\right) at\ low\ [NO]$$

<div align="right">Equation 3</div>

The activated state for *Ns* H-NOX appears to be the hexacoordinate ON-heme-N* species in Scheme I, with the nitrogen base being unknown, but presumed to be a histidyl side chain, possibly the distal amino acid, His150. Although *Ns* H-NOX does not form a fully 5c NO-heme species, a major conformational change in the protein does appear to be induced by transient binding of a second NO as is observed for sGC, and perhaps the conformation change in the activated, six coordinate ON-heme-N* state of H-NOX is more similar to that observed in sGC than is apparent from spectral analyses of the iron complexes.

(4) *Ns* H-NOX heme is sensitive to atmospheric oxygen and autooxidizes over a period of 24 hours, but no Fe(II)O$_2$ intermediate is ever observed. In contrast, full-length sGC is inert to reactions with O$_2$ in air or at 1 atm of the pure gas. However, truncated $\beta1$ corresponding to the H-NOX domain readily autooxidizes at rates of 4.3 hr^{-1} and 0.18 hr^{-1} at 37 °C, respectively, for ferrous $\beta1(1–194)$ and $\beta2(1–217)$ mutant sGC (39). These autooxidation rates are much greater than those of mammalian HbO$_2$, MbO$_2$ and reduced *Ns* H-NOX, indicating that the deleted ~400 residues of sGC β-subunit or perhaps the alpha subunit protects the ferrous heme from autooxidation (24).

(5) The majority of the heme in oxidized *Ns* H-NOX is 6c low-spin rather than the pure high-spin 5c form found for sGC (14,38,40). There appears to be reversible ligation and dissociation of an endogenous distal ligand, perhaps His150, during redox cycling in *Ns* H-NOX. Similar experiments with sGC indicate the proximal His remains bound in both the

oxidized and reduced forms, but reversible dissociation of the proximal histidine does occur after NO binding to the ferrous form of sGC to create the activated 5c NO complex..

(6) *Ns* H-NOX reacts 100-fold more rapidly with CO than sGC and has a much higher affinity for this ligand, implying that the iron atom is more reactive in the bacterial sensor (41). However, the bimolecular rate constants for NO binding to form the first 6c NO-heme-His complexes are nearly identical, very large (100–300 $\mu M^{-1}s^{-1}$), and probably diffusion controlled, implying little resistance to ligand movement into both proteins.

NO binding to *Ns* H-NOX was examined previously in different way by Boon et al. (42). In their study, the sensor protein was first treated with excess of NO releaser (NONOate), diethylamine and then gel-filtered to remove all side products of NONOate and free NO. Spectral studies and dissociation kinetics were assessed using this NO complex of H-NOX (42). Optical and resonance Raman spectra indicated that both 5c and 6c NO complexes were present (42) and the amount of 5c component (40–50%) was similar to what we observed in the presence of excess amount of NO (Fig. 3a, lower panel). However, in our study when a stoichiometric amount of NO was added to *Ns* H-NOX only a 6c NO complex with a Soret absorption peak at 418 nm is formed and is stable for several hours. Thus, *Ns* H-NOX adopts different coordination geometries at 1:1 versus excess NO levels. This observation is most readily interpreted using the multiple-step mechanism for NO binding shown in Scheme I. In principle, this simple hexacoordinate ON-heme-His complex should equilibrate to the final ON-heme-N*/ON-heme mixture, but catalytic amounts of excess NO are needed to facilitate this transition on normal time scales after preparation. Although Boon et al. removed free NO from their final sample via gel filtration, excess NO was almost certainly present during the prolonged incubation of the NONOate with the sensor protein.

Boon et al. also reported that they were unable to measure NO dissociation from *Ns* H-NOX using either excess CO (plus 30 mM dithionite) or HbO2, whereas the same methods enabled successful determinations for NO dissociation rate constant for other two H-NOX proteins (42). In contrast, we were able to measure NO dissociation from the initial 6c NO complex of *Ns* H-NOX (Fig. 4b). Thus, the equilibrium mixture of 6c and 5c species for the NO H-NOX complex prepared in the presence of excess NO appears to have much lower NO dissociation rate constants. However, a more careful study of NO dissociation is needed to resolve the exact kinetic properties of the initial 6c, 418 nm; the intermediate 6c, 414nm; and the 5c, 399 nm NO H-NOX complexes.

Structural interpretations

We had previously observed that NO binding to *Ns* H-NOX yields only ~40% population of 5c NO-heme compared to sGC, and proposed a possible structural basis for this difference (14). The *Ns* H-NOX heme-pocket residues Met144 and Trp74 are larger than the spatially analogous isoleucine and phenylalanine residues in sGC and might be inhibiting stable formation of a 5c NO-heme complex. We subsequently generated M144I and the W74F mutants of *Ns* H-NOX, engineering the heme pocket to be similar to sGC. Both single mutations resulted in larger populations of 5c NO-heme complexes, as indicated by their optical spectra (14). To extend these observations, we prepared the NO complex of reduced M144I H-NOX (generated either by adding excess NO or reacting sodium nitrite with dithionite), and as shown in Fig. 6 (top solid spectrum), this mutant in excess NO exhibits a pure low spin 5c NO-heme EPR spectrum, which is characteristic of only a single axial N atom with pronounced 3 hyperfine lines with a splitting constant of 17 G caused by the nitrogen nucleus of the proximal ligand, His105. This spectrum is very similar to that observed for the NO complex of the reduced sGC (38). Indeed, the EPR spectrum can be properly simulated by parameters as a nearly axial low-spin 5c NO complex (Fig. 6, top

dashed spectrum). This effect led us to speculate instead that *Ns* H-NOX might be more sensitized to a transition to 5c NO-heme once it is bound to its effector domain. Replacement of Met144 with Ile does appear to make the behavior of *Ns* H-NOX closer to that of sGC in terms of NO binding and perhaps sensing in the ferrous state. Thus, introduction of a methionine in place of the isoleucine in the *Ns* H-NOX may be an adaptation to a different functional role, such as sensing the redox potential of the environment.

A "heme pivoting" model for sGC was proposed to interpret 5c NO-heme formation, activation of the cyclase, and other fast relaxation events after NO binding to the heme sensor domain (14,43). In the case of *Ns* H-NOX, oxidation produces a 6c low spin complex that appears to require a substantially larger conformational change than that postulated "heme pivoting and bending" mechanism of sGC, where side chain motions of < 2 Å are proposed to occur in response to gaseous ligand binding (14). The large motions triggered by oxidation are required for the coordination of all the possible axial ligands of ferric *Ns* H-NOX, and particularly for His150. His150 is the closest histidine residue to the heme in the crystallographic structure of the ferrous H-NOX but is still 17.6 Å away from the iron atom (14). The heme moiety is located in the interface of the proximal αββαββ domain and the distal α-helical domain, and movement of a His150 to become an axial ligand would require "melting" of a significant percentage of α-helical secondary structure. This interpretation is consistent with the loss of ellipticity at 222 nm seen after oxidation of H-NOX (Fig. 11). Attempts to crystallize ferric H-NOX have not been successful perhaps reflecting the conformational flexibility required for bis-histidyl coordination.

Our current EPR, NIR MCD analysis and the published crystallographic data (14) for *Ns* H-NOX show little 5c NO-heme formation at low [NO], implying an activation mechanism different from that for sGC. However, as suggested in Schemes I and II and observed experimentally, the secondary spectral and conformational changes following formation of the initial 6c NO-heme-His complex in both proteins depends linearly on [NO] and appear to be catalyzed by transient formation of NO-heme-NO complexes (28). Thus, it is possible that the early stage protein conformational changes of sGC and *Ns* H-NOX are similar and driven by this unusual bis-NO heme chemistry.

The structure of the second 6c-NO complex in *Ns* H-NOX with an absorption peak at 414 nm is not resolved, but both the optical and EPR characterizations provided useful clue about its structure. Although the Soret peak is at the same wavelength, it is not the ferric form of the sensor, because the lineshape of the peaks in the visible region and near UV region are different (compare Figs. 1 and 3a), and this 414 nm NO-heme species has a large g=2 EPR signal with typical hyperfine nine line features indicative of ferrous ON-heme-His complexes. It cannot be a bis-nitrosyl ferrous heme intermediate, which is an EPR-silent diamagnetic species. The initial 6c NO-heme-His complex in *Ns* H-NOX is also well defined spectrally by a nine-line g=2 EPR signal and is identical to the EPR spectrum of the initial complex formed in sGC. In the latter case, this 6c signal changes to a three-line g=2 signal characteristic of a 5c NO-heme complex even at 1:1 NO/Heme. The very similar EPR spectra of the NO complex of *Ns* H-NOX containing 1:1 and 2:1 NO strongly support that these two 6c NO complexes, one with a peak at 418 and the other at 414 nm, have His-heme-NO coordination with the former having the proximal His105 and the latter perhaps the distal His150 as the heme axial ligands, i.e., the mechanism proposed in Scheme I.

A second NO molecule has also been postulated to bind to the sGC heme iron as a proximal ligand or at a non-heme site during the activation process (43–46). However, a site other than the heme iron is hard to justify for the fast NO binding rate because cysteine nitrosothiol formation will not occur anaerobically, and even the nitrosation reaction

mediated by oxygen is very slow (47). There is no additional metal center adjacent to the heme iron that could be a second NO target. In our view, the NO concentration dependence of the 6c to 5c transition in sGC is most readily explained by formation of a transient ON-heme-NO complex as shown in Scheme II, and a similar bis-NO heme complex appears to be required for the transition from the 418 to 414 nm 6c NO-heme-His species in *Ns* H-NOX. Finally, the formation of a bis-axial ligand complex clearly occurs when H-NOX is oxidized and must involve substantial conformational changes regardless of the identification of the second ligand. Thus, hexacoordination of H-NOX is clearly a key part of the triggering mechanism for signaling by this sensor and can be produced by either NO binding or oxidation.

Physiological function of H-NOX

The biological function of H-NOX in *Nostoc sp* remains unresolved because the "effector" component for this sensor has not been found. This symbiotic cyanobacterium can perform both anaerobic nitrogen fixation and oxygen evolving photosynthesis (48). These two mechanisms of energy metabolism are not compatible, and the bacteria have developed specialized cells called heterocysts to isolate the machinery for nitrogen fixation from oxygen-evolving photosynthesis. Special mechanisms must have evolved in these organisms to protect against oxidative and light stress.

Proteomic analysis of the soluble fraction of the *Nostoc sp* has revealed many, perhaps redundant proteins that appear to sense and respond to the environmental changes and stresses (48). Multiple copies of superoxide dismutase, catalase, peroxiredoxin and peroxidase are expressed to metabolize superoxide and peroxides. Several glutathione metabolizing enzymes are present in abundance to maintain the steady-state level of cellular glutathione and regulate the overall cellular redox potential. Most of these major protein components appear to have evolved to counter oxidative stress. Thus, in addition to binding diatomic gases, *Ns* H-NOX might be sensing redox state changes and triggering its transducer to achieve feedback regulation of the cellular redox potential. Such a function appears to occur for the H-NOX sensor from *Shewanella oneidensi* (49). This H-NOX is coupled to a histidine kinase to sense environmental changes in oxygen levels. Since NO-bound H-NOX cannot be readily oxidized, retained NO binding capability can further serve to isolate nitrogen fixation and oxygen-evolving machinery by firmly setting this particular effector switch to "off" at high NO concentrations. Oxidation of sGC under pathophysiological conditions leads to ubiquitin-dependent degradation and may be a mechanism for deactivation of sGC (16). The switch between oxidative degradation of sGC and NO activation may have evolved from the proposed switch between NO sensing and redox sensing that we suggest may occur for *Ns* H-NOX.

Abbreviations

NO	nitric oxide
CO	carbon monoxide
H-NOX	Heme-Nitric oxide and OXygen binding
Ns **H-NOX**	*Nostoc sp* H-NOX
Tt **H-NOX**	*Thermoanaerobacter tengcongensis* H-NOX
sGC	Soluble guanylyl cyclase
DTT	dithiothreitol
β-BME	mercaptoethanol

IPTG	isopropyl-1-thio-β-D-galactopyranoside
PMSF	phenylmethyl-sulfonyl fluoride
Hbs	hemoglobin
Mbs	myoglobin
HbO$_2$	oxyhemoglobin
MbO$_2$	oxymyoglobin
CD	circular dichroism
MCD	Magnetic Circular Dichroism
NIR MCD	near infrared MCD
EPR	electron Electron Paramagnetic Resonance spectroscopy
Fe(II)	ferrous heme
Fe(III)	ferric heme
5c-NO	five coordinate NO-heme complex
6c-NO	six coordinate NO-heme complex
NONOate	NO releaser

References

1. Bertini, I.; Sigel, A.; Sigel, H., editors. Handbooks on metalloproteins. New York: Marcel Dekker, Inc.; 2001.

2. Kadish, KM.; Smith, KM.; Guilard, R., editors. The Porphyrin Handbook. Vol. Vol. 4, 8, 11. Amsterdam: Academic Press; 2000.

3. Messerschmidt, A.; Huber, R.; Poulos, T.; Wieghardt, K., editors. Handbooks of metalloproteins. Vol. Vol. 1. Chichester: John Wiley and Sons, Ltd; 2001.

4. Gilles-Gonzalez MA, Gonzalez G. Heme-based sensors: defining characteristics, recent developments, and regulatory hypotheses. J Inorg Biochem. 2005; 99:1–22. [PubMed: 15598487]

5. Jain R, Chan MK. Mechanisms of ligand discrimination by heme proteins. J Biol Inorg Chem. 2003; 8:1–11. [PubMed: 12459893]

6. Olson JS, Phillips GN Jr. Kinetic Pathways and Barriers for Ligand Binding to Myoglobin. J Biol Chem. 1996; 271:17596. [PubMed: 8663556]

7. Boon EM, Marletta MA. Ligand discrimination in soluble guanylate cyclase and the H-NOX family of heme sensor proteins. Curr Opin Chem Biol. 2005; 9:441–446. [PubMed: 16125437]

8. Iyer LM, Anantharaman V, Aravind L. Ancient conserved domains shared by animal soluble guanylyl cyclases and bacterial signaling proteins. BMC Genomics. 2003; 4:5. [PubMed: 12590654]

9. Aono S. Metal-containing sensor proteins sensing diatomic gas molecules. Dalton Trans. 2008:3137–3146. [PubMed: 18688409]

10. Derbyshire ER, Marletta MA. Biochemistry of soluble guanylate cyclase. Handb Exp Pharmacol. 2009:17–31. [PubMed: 19089323]

11. Koesling D, Russwurm M, Mergia E, Mullershausen F, Friebe A. Nitric oxide-sensitive guanylyl cyclase: structure and regulation. Neurochem Int. 2004; 45:813–819. [PubMed: 15312975]

12. Nioche P, Berka V, Vipond J, Minton N, Tsai AL, Raman CS. Femtomolar sensitivity of a NO sensor from Clostridium botulinum. Science. 2004; 306:1550–1553. [PubMed: 15472039]

13. Pellicena P, Karow DS, Boon EM, Marletta MA, Kuriyan J. Crystal structure of an oxygen-binding heme domain related to soluble guanylate cyclases. Proc Natl Acad Sci U S A. 2004; 101:12854–12859. [PubMed: 15326296]

14. Ma X, Sayed N, Beuve A, van den Akker F. NO and CO differentially activate soluble guanylyl cyclase via a heme pivot-bend mechanism. Embo J. 2007; 26:578–588. [PubMed: 17215864]

15. Stasch JP, Schmidt P, Alonso-Alija C, Apeler H, Dembowsky K, Haerter M, Heil M, Minuth T, Perzborn E, Pleiss U, Schramm M, Schroeder W, Schroder H, Stahl E, Steinke W, Wunder F. NO- and haem-independent activation of soluble guanylyl cyclase: molecular basis and cardiovascular implications of a new pharmacological principle. Br J Pharmacol. 2002; 136:773–783. [PubMed: 12086987]

16. Evgenov OV, Pacher P, Schmidt PM, Hasko G, Schmidt HH, Stasch JP. NO-independent stimulators and activators of soluble guanylate cyclase: discovery and therapeutic potential. Nat Rev Drug Discov. 2006; 5:755–768. [PubMed: 16955067]

17. Meurer S, Pioch S, Pabst T, Opitz N, Schmidt PM, Beckhaus T, Wagner K, Matt S, Gegenbauer K, Geschka S, Karas M, Stasch JP, Schmidt HH, Muller-Esterl W. Nitric oxide-independent vasodilator rescues heme-oxidized soluble guanylate cyclase from proteasomal degradation. Circ Res. 2009; 105:33–41. [PubMed: 19478201]

18. Smith PK, Krohn RI, Hermanson GT, Mallia AK, Gartner FH, Provenzano MD, Fujimoto EK, Goeke NM, Olson BJ, Klenk DC. Measurement of protein using bicinchoninic acid. Anal Biochem. 1985; 150:76–85. [PubMed: 3843705]

19. Berka V, Palmer G, Chen PF, Tsai A-L. Effects of various imidazole ligands on heme conformation in endothelial nitric oxide synthase. Biochemistry. 1998; 37:6136–6144. [PubMed: 9558353]

20. Berka V, Tsai A-L. Characterization of interactions among the heme center, tetrahydrobiopterin, and L-arginine binding sites of ferric eNOS using imidazole, cyanide, and nitric oxide as probes. Biochemistry. 2000; 39:9373–9383. [PubMed: 10924132]

21. Salter MD, Nienhaus K, Nienhaus GU, Dewilde S, Moens L, Pesce A, Nardini M, Bolognesi M, Olson JS. The apolar channel in Cerebratulus lacteus hemoglobin is the route for O2 entry and exit. J Biol Chem. 2008; 283:35689–35702. [PubMed: 18840607]

22. Du M, Yeh HC, Berka V, Wang LH, Tsai A-L. Redox properties of human endothelial nitric-oxide synthase oxygenase and reductase domains purified from yeast expression system. J Biol Chem. 2003; 278:6002–6011. [PubMed: 12480940]

23. Tsai A-L, Berka V, Chen PF, Palmer G. Characterization of endothelial nitric-oxide synthase and its reaction with ligand by electron paramagnetic resonance spectroscopy. J Biol Chem. 1996; 271:32563–32571. [PubMed: 8955082]

24. Stone JR, Marletta MA. Soluble guanylate cyclase from bovine lung: activation with nitric oxide and carbon monoxide and spectral characterization of the ferrous and ferric states. Biochemistry. 1994; 33:5636–5640. [PubMed: 7910035]

25. Brantley RE Jr, Smerdon SJ, Wilkinson AJ, Singleton EW, Olson JS. The mechanism of autooxidation of myoglobin. J Biol Chem. 1993; 268:6995–7010. [PubMed: 8463233]

26. Yasuda J, Ichikawa T, Tsuruga M, Matsuoka A, Sugawara Y, Shikama K. The alpha 1 beta 1 contact of human hemoglobin plays a key role in stabilizing the bound dioxygen. Eur J Biochem. 2002; 269:202–211. [PubMed: 11784314]

27. Martin E, Berka V, Bogatenkova E, Murad F, Tsai AL. Ligand selectivity of soluble guanylyl cyclase: Effect of the hydrogen bonding tyrosine in the distal heme pocket on binding of oxygen, nitric oxide and carbon monoxide. J Biol Chem. 2006

28. Zhao Y, Brandish PE, Ballou DP, Marletta MA. A molecular basis for nitric oxide sensing by soluble guanylate cyclase. Proc Natl Acad Sci U S A. 1999; 96:14753–14758. [PubMed: 10611285]

29. Kharitonov VG, Sharma VS, Magde D, Koesling D. Kinetics of nitric oxide dissociation from five- and six-coordinate nitrosyl hemes and heme proteins, including soluble guanylate cyclase. Biochemistry. 1997; 36:6814–6818. [PubMed: 9184164]

30. John S, Olson 7 George N, Phillips J. Myoglobin discriminates between O2, NO, and CO by electrostatic interactions with the bound ligand. J. Biol. Inorg. Chem. 1997; 2:544–552.

31. Palmer, G. Electron paramagnetic resonance of metalloproteins. Sausalito, CA: University Science Books; 2000.

32. Tsai A-L, Kulmacz RJ, Wang JS, Wang Y, Van Wart HE, Palmer G. Heme coordination of prostaglandin H synthase. J Biol Chem. 1993; 268:8554–8563. [PubMed: 8386163]

33. Blumberg WE, Peisach J. Low-spin compounds of heme proteins. Adv. Chem. Ser. 1971; 100:271–291.

34. Cheesman MR, Greenwood C, Thomson AJ. Magnetic circular dichroism of hemoproteins. Adv. Inorg. Chem. 1991; 36:201–255.

35. Gadsby PM, Peterson J, Foote N, Greenwood C, Thomson AJ. Identification of the ligand-exchange process in the alkaline transition of horse heart cytochrome c. Biochem J. 1987; 246:43–54. [PubMed: 2823795]

36. Rigby SE, Moore GR, Gray JC, Gadsby PM, George SJ, Thomson AJ. N.m.r., e.p.r. and magnetic-c.d. studies of cytochrome f. Identity of the haem axial ligands. Biochem J. 1988; 256:571–577. [PubMed: 3223931]

37. Moore GR, Williams RJ, Peterson J, Thomson AJ, Mathews FS. A spectroscopic investigation of the structure and redox properties of Escherichia coli cytochrome b-562. Biochim Biophys Acta. 1985; 829:83–96. [PubMed: 2986699]

38. Martin E, Berka V, Tsai AL, Murad F. Soluble guanylyl cyclase: the nitric oxide receptor. Methods Enzymol. 2005; 396:478–492. [PubMed: 16291255]

39. Karow DS, Pan D, Davis JH, Behrends S, Mathies RA, Marletta MA. Characterization of functional heme domains from soluble guanylate cyclase. Biochemistry. 2005; 44:16266–16274. [PubMed: 16331987]

40. Stone JR, Sands RH, Dunham WR, Marletta MA. Spectral and ligand-binding properties of an unusual hemoprotein, the ferric form of soluble guanylate cyclase. Biochemistry. 1996; 35:3258–3262. [PubMed: 8605161]

41. Hoshino M, Ozawa K, Seki H, Ford PC. Photochemistry of nitric oxide adducts of water-soluble iron(III) porphyrin and ferrihemoproteins studied by nanosecond laser photolysis. J Am Chem Soc. 1993; 115:9568–9575.

42. Boon EM, Davis JH, Tran R, Karow DS, Huang SH, Pan D, Miazgowicz MM, Mathies RA, Marletta MA. Nitric oxide binding to prokaryotic homologs of the soluble guanylate cyclase beta1 H-NOX domain. J Biol Chem. 2006; 281:21892–21902. [PubMed: 16728401]

43. Sayed N, Baskaran P, Ma X, van den Akker F, Beuve A. Desensitization of soluble guanylyl cyclase, the NO receptor, by S-nitrosylation. Proc Natl Acad Sci U S A. 2007; 104:12312–12317. [PubMed: 17636120]

44. Russwurm M, Koesling D. NO activation of guanylyl cyclase. Embo J. 2004; 23:4443–4450. [PubMed: 15510222]

45. Russwurm M, Koesling D. Guanylyl cyclase: NO hits its target. Biochem Soc Symp. 2004:51–63. [PubMed: 15777012]

46. Cary SP, Winger JA, Derbyshire ER, Marletta MA. Nitric oxide signaling: no longer simply on or off. Trends Biochem Sci. 2006; 31:231–239. [PubMed: 16530415]

47. Kharitonov VG, Sundquist AR, Sharma VS. Kinetics of nitrosation of thiols by nitric oxide in the presence of oxygen. J Biol Chem. 1995; 270:28158–28164. [PubMed: 7499306]

48. Anderson DC, Campbell EL, Meeks JC. A soluble 3D LC/MS/MS proteome of the filamentous cyanobacterium Nostoc punctiforme. J Proteome Res. 2006; 5:3096–3104. [PubMed: 17081061]

49. Price MS, Chao LY, Marletta MA. Shewanella oneidensis MR-1 H-NOX regulation of a histidine kinase by nitric oxide. Biochemistry. 2007; 46:13677–13683. [PubMed: 17988156]

50. Zhao Y, Brandish PE, Ballou DP, Marletta MA. A molecular basis for nitric oxide sensing by soluble guanylate cyclase. Proc Natl Acad Sci U S A. 1999; 96:14753–14758. [PubMed: 10611285]

51. Peisach J, Blumberg WE, Lode ET, Coon MJ. An analysis of the electron paramagnetic resonance spectrum of pseudomonas oleovorans rubredoxin. A method for determination of the ligands of ferric iron in completely rhombic sites. J Biol Chem. 1971; 246:5877–5881. [PubMed: 4330058]

52. Muller B, Kleschyov AL, Stoclet JC. Evidence for N-acetylcysteine-sensitive nitric oxide storage as dinitrosyl-iron complexes in lipopolysaccharide-treated rat aorta. Br J Pharmacol. 1996; 119:1281–1285. [PubMed: 8937735]
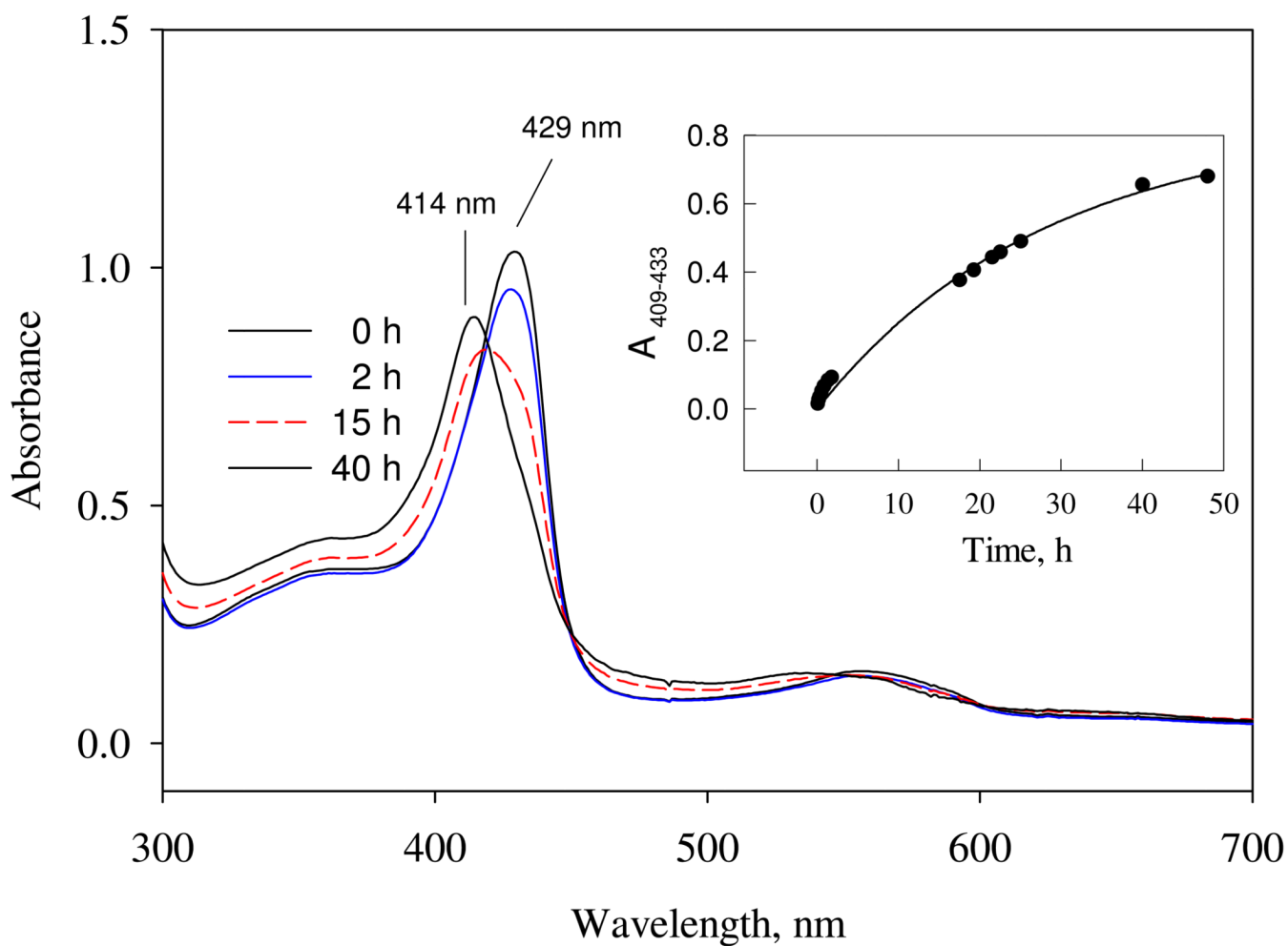
Figure 1.
Kinetics of autooxidation of ferrous *Ns* H-NOX. 6 µM of ferrous *Ns* H-NOX in the absence of DTT was placed in the HP8453 diode array spectrophotometer to follow the optical changes up to 2 days at 24 °C. The kinetics of $\Delta A_{409-443}$ was fit to one-exponential function to obtain the rate of autooxidation (Inset).
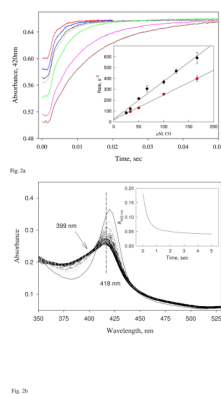
Figure 2.
A: Kinetics of CO binding to the ferrous *Ns* H-NOX. Ferrous *Ns* H-NOX, 5 µM, prepared in an anaerobic tonometer was reacted with CO in a stopped-flow at 24 °C. CO was prepared in anaerobic buffer at concentrations varying from 25 to 166 µM. One-exponential change of absorbance at 420 nm was used to determine the observed rates and used for calculation of the 2nd-order on rate constant (Inset). Two sets of experiments using two different batches of sensor protein were conducted (red and black circles). Standard deviation of at least triplicates at each concentration was shown by the significant bar. **B: Determination of the dissociation rate constant of CO binding**. CO-ferrous *Ns* H-NOX complex was pre-formed by mixing 4 µM sensor with 1 mM CO in an anaerobic glass tonometer, and then reacted with 1 mM NO solution. The CO-dissociation rate was followed by diode array or single wavelength stopped-flow at 422 nm (Inset) for 8s data collection at 24 °C. Kinetic data were fit to 2- exponential function.
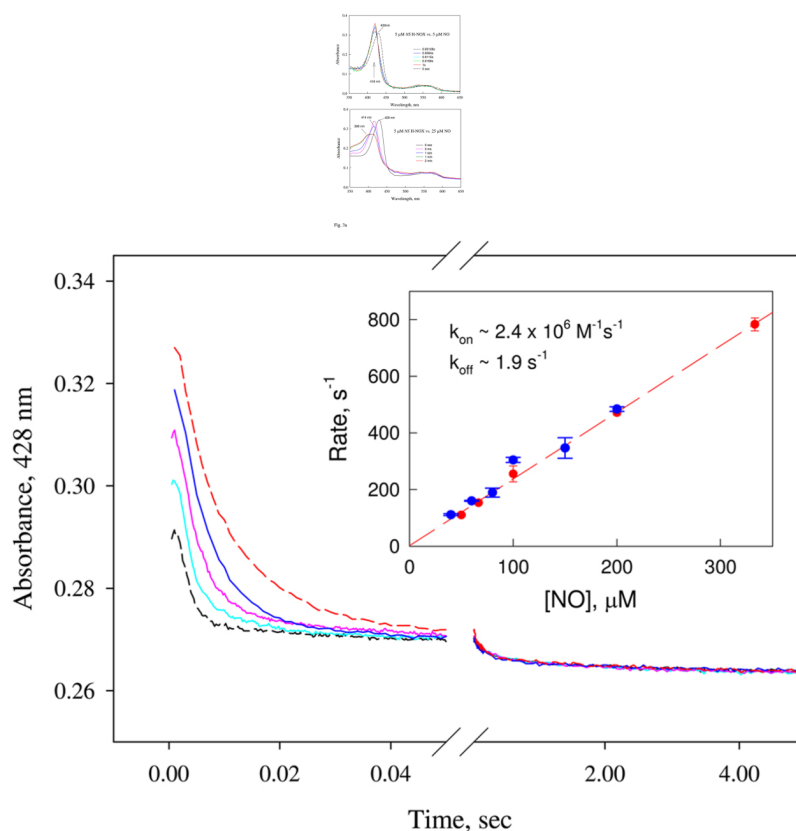
Fig. 3b

Figure 3.
A: Optical characterization of *Ns* H-NOX binding to stoichiometric and excess amount of NO. UV-Vis spectral changes recorded by anaerobic rapid-scan diode array stopped-flow within 1 s or 2 min for 5 μM *Ns* H-NOX reaction with 1:1 and 5:1 ratio of NO, respectively, at 24 °C. **B: Kinetics of *Ns* H-NOX binding with excess NO under pseudo first-order conditions**. 5 μM ferrous *Ns* H-NOX was mixed with > 10 × of NO at different concentrations and the kinetics was recorded by single wavelength stopped-flow at 428 nm at 50 ms/ 5s split time mode to cover the triphasic changes. Data were fit by 3-exponential function and the first fast phase that show [NO] dependence was further analyzed to obtain the 2nd order binding rate constant as the secondary plot (Inset). Average of three shots or more with the standard deviation plotted as the error bar for each NO concentration in two different sets of experiments (blue and red symbols). The linear regression (red dash) and the slope and y-intercept obtained are that with one of the two sets of data.
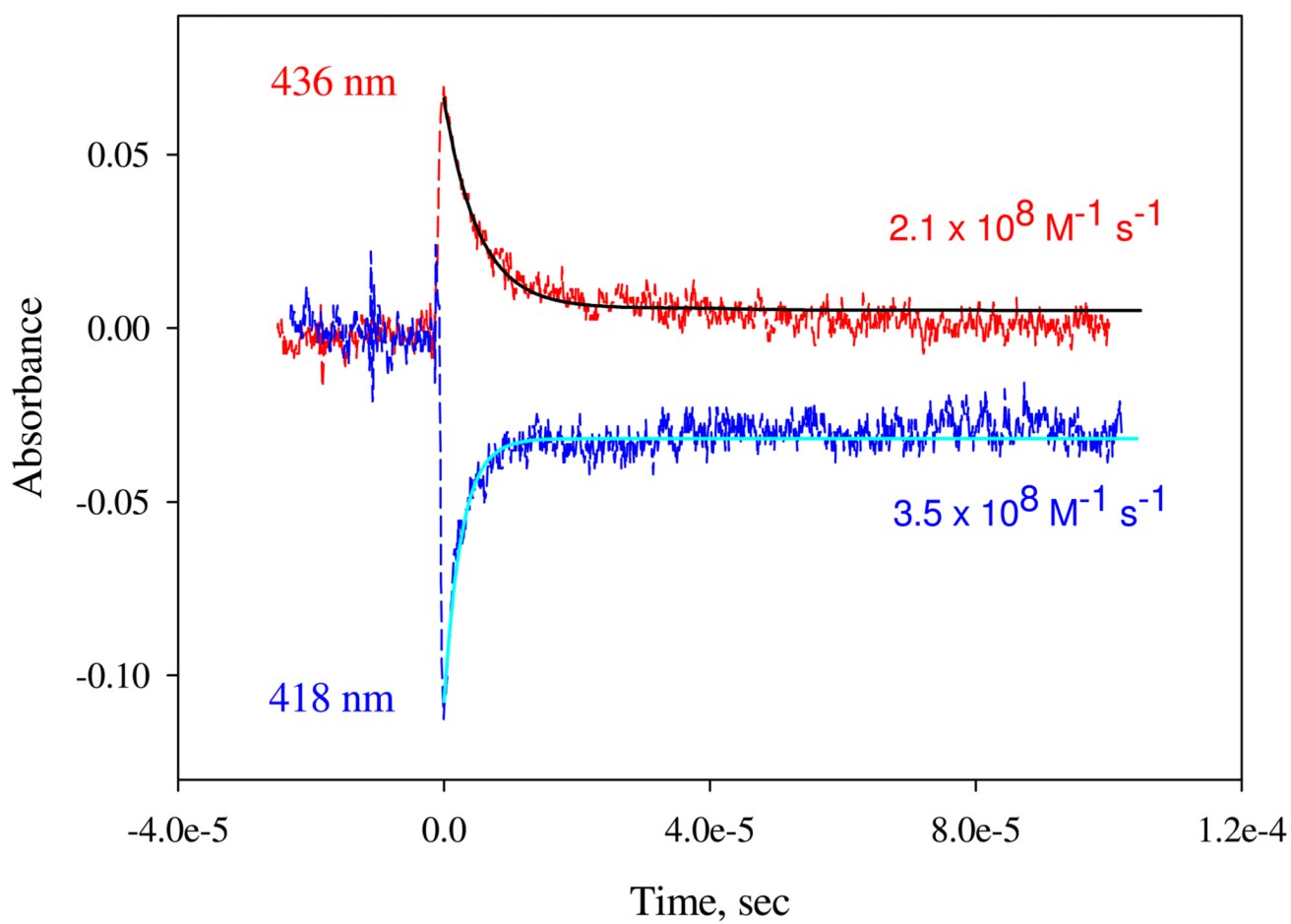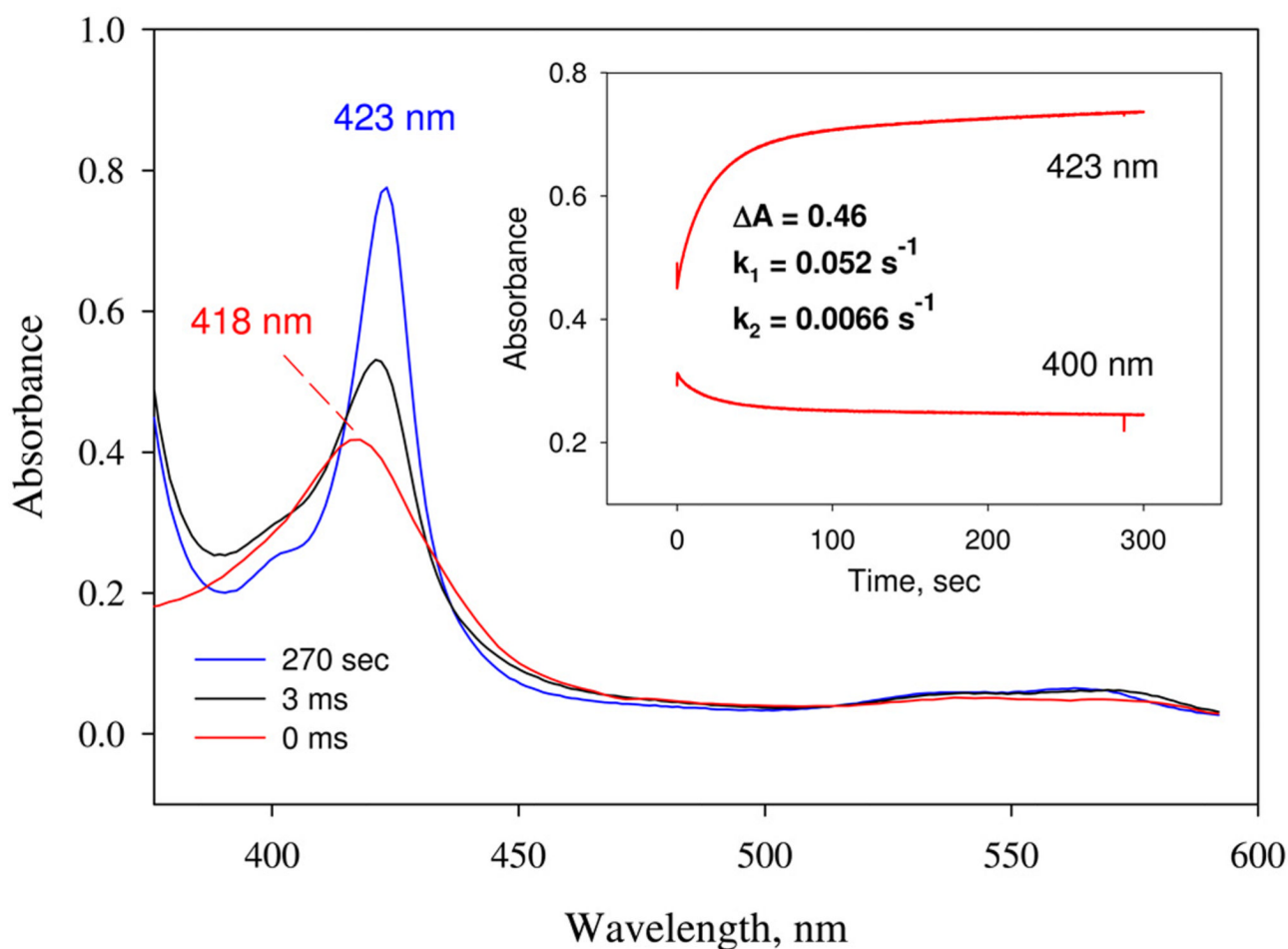
Fig. 4a

Fig. 4b

Figure 4.
Determination of the association (A) and dissociation (B) rate constants of NO binding to *Ns* H-NOX for formation of the 1st 6c NO complex by flow-flash and stopped-flow. A: CO complex of *Ns* H-NOX was first prepared with 50 µM sensor protein and 100 µM CO anaerobically in a syringe. This complex was briefly mixed with 1 mM NO in the stopped-flow for 50 ms and a 0.5 µs 577 nm dye laser was applied to flash off the bound CO. Subsequent NO association kinetics was monitored at both 436 (red trace) and 418 nm (blue trace). Black lines are one-exponential fittings for both data. **B**: NO complex of *Ns* H-NOX was first prepared anaerobically by mixing 5 µM sensor protein with 10 µM NO in a glass tonometer. This mixture was then mixed with a mixture of 1 mM CO and 25 mM dithionite and aged for 50 ms in a rapid scan stopped-flow and the electronic absorption spectra at 3 ms (black) and 270 s (blue) were shown together with that at zero time. Single wavelength kinetic data at 428 and 400 nm with opposite amplitude changes are shown in the Inset and fit to 1-exponential function to obtain the rate constant. All reactions were conducted at 20 °C.
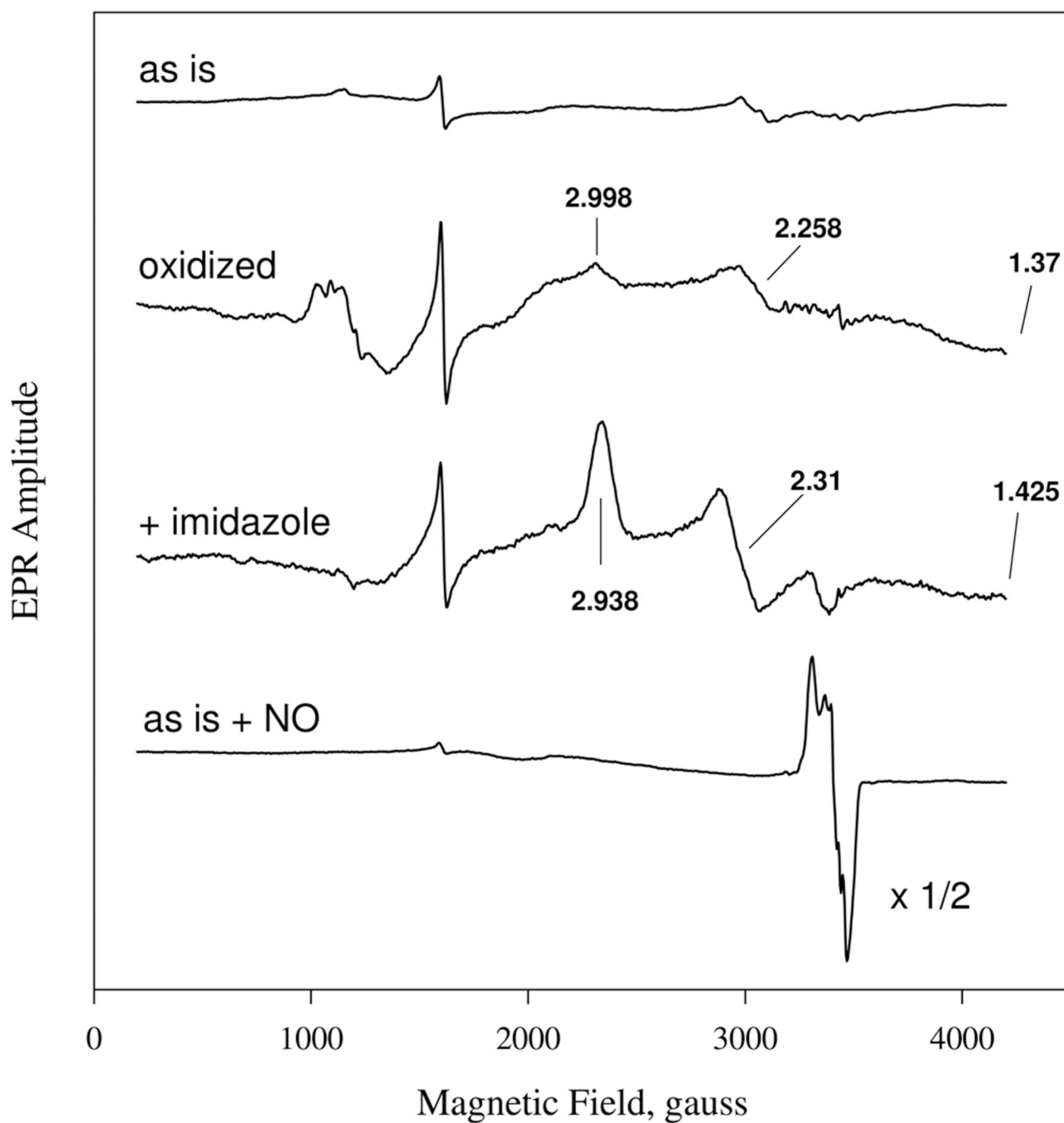
Figure 5.
EPR spectra of *Ns* H-NOX at different redox state and coordination. EPR spectra are presented (from top to bottom) for 80 µM isolated ferrous *Ns* H-NOX, 55 µM ferric *Ns* H-NOX prepared by ferricyanide oxidation and gel-filtration chromatography, 50 µM ferric *Ns* H-NOX mixed with 50 mM imidazole, and ferrous NO complex formed with 160 µM NO. EPR conditions were: 4 mW, 9.602 gHz, time constant: 0.33s, modulation amplitude: 10.9G and 10K.
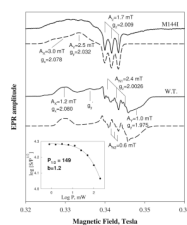
Figure 6.
EPR characterization of the ferrous NO complex of *Ns* H-NOX. 70 µM ferrous *Ns* H-NOX was reacted with 2:1 NO by injecting 2 mM NO-saturated buffer under anaerobic condition and manually frozen for EPR assessment (bottom solid trace). The hyperfine splitting by NO nitrogen nucleus and super hyperfine splitting by the proximal histidine were indicated for the g_z component as well as the isotropic hyperfine splitting for the g_y and g_x component optimized via spectral simulation to the dominant 6c low-spin NO complex (bottom dashed trace). An EPR for 60 µM ferrous NO complex of M144I sensor dominated by 5c NO complex was juxtaposed for comparison (top solid trace). The three g values and the associated hyperfine parameter values for a simulated 5c-NO complex spectrum (top dashed trace) that closely matches the acquired spectrum are also indicated for comparison with those obtained for the wild type sensor. Progressive power saturation at LN temperature, the value of half-saturation power, $P_{1/2}$, and value of b by fitting the data to equation (2) are also shown for the wild type sample (Inset). EPR conditions were the same as described in Fig. 5 except 1.87 G modulation amplitude and 9.28 gHz frequency.
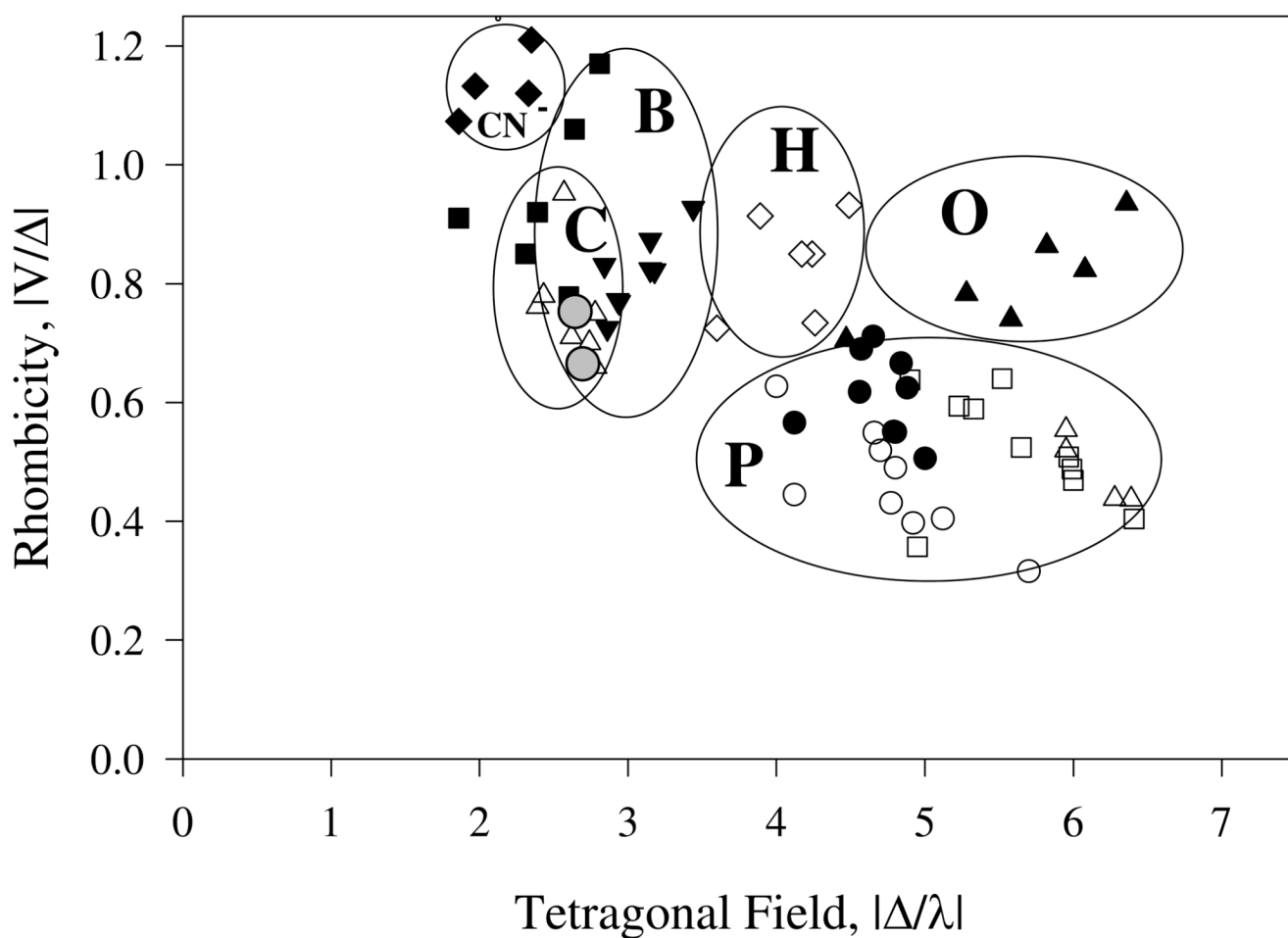
Figure 7.
Truth diagram analysis of the low-spin ferric *Ns* H-NOX and its imidazole complex.
Correlation between the heme rhombicity and the axial ligand strength of many low-spin
heme complexes (various symbols) are mapped in six different zones. Complexes in five of
them have histidine as proximal ligand and with cyanide (zone CN−), methionine (zone C),
histidine (zone B), histidinate/azide (zone H), and hydroxide/phenolate (zone O) as the distal
ligand. Those hemeprotein containing a cysteine thiolate proximal ligand including P450,
chloroperoxidase and nitric oxide synthase and their derivatives fall in the P zone. This
diagram was modified from the original Blumberg Peisach convention (33,51). The grey
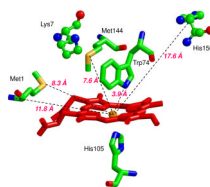solid circles are the ferric *Ns* H-NOX and its imidazole derivative.

Figure 8.
Candidate axial heme ligand for ferric *Ns* H-NOX. Potential heme-ligand residues nearby heme iron and at the distal heme side of the wild type ferrous *Ns* H-NOX are displayed. Distances between two candidate methionine residues (Met144 and Met1), N-terminal amino group, Trp74 indole nitrogen and the heme iron (orange ball) are given. The second closest histidine, His150 and the closest lysine, Lys7 and the proximal heme ligand, His105, are also shown in stick model. Heme porphyrin is shown as red stick model. This is a RASMOL representation of PDB identifier: 2O09.
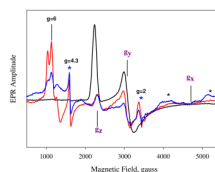
Figure 9.
Similarity of EPR spectrum between *Ns* H-NOX and cytochrome c. **EPR of 65 µM**
ferric *Ns* H-NOX (red), 30 µM M144I *Ns* H-NOX (blue), and 500 µM bovine cytochrome c
(black) are directly compared for the position of the principal g values of the low-spin
rhombic heme. The additional features including the high-spin heme at g = 6 region and the
non-specific iron at g = 4.3 and organic radical at g = 2 present in the *Ns* H-NOX are not
present in cytochrome c. The two broad features highlighted by the red stars are artifacts of
the resonator. The EPR amplitude for the M144I mutant has been adjusted for its
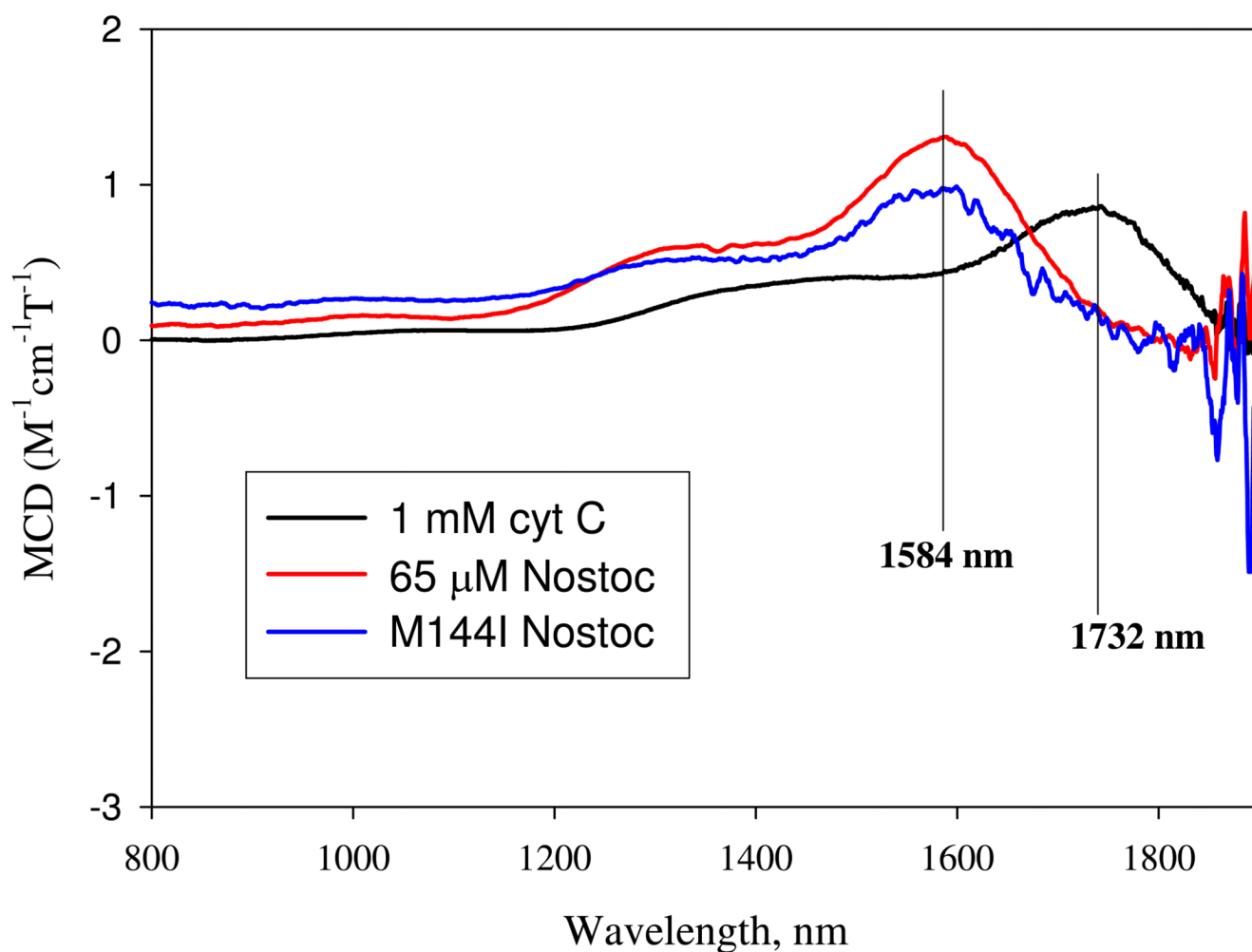concentration difference from the wild type sample.

Figure 10.
Identification of the axial heme ligands of ferric *Ns* H-NOX by NIR MCD. Same three samples used for EPR measurements in Fig. 9 were used in the NIR MCD measurements in the range from 800 to 2000 nm at 24 °C. All samples were prepared in D_2O 50 mM HEPES, pH 7.4 to minimize the NIR MCD overtone background signals from the water solvent (34). MCD conditions are described in the Methods and the spectrum for cytochrome c was obtained as one scan while that of wild type and M144I *Ns* H-NOX were an average of 8 scans. The wavelengths of the main transitions are labeled for each sample. These marker wavelengths (nm), or energy levels are used to identify the axial ligand pairs from the correlation diagram composed for a series of low-spin hemeproteins with two axial ligands (34).
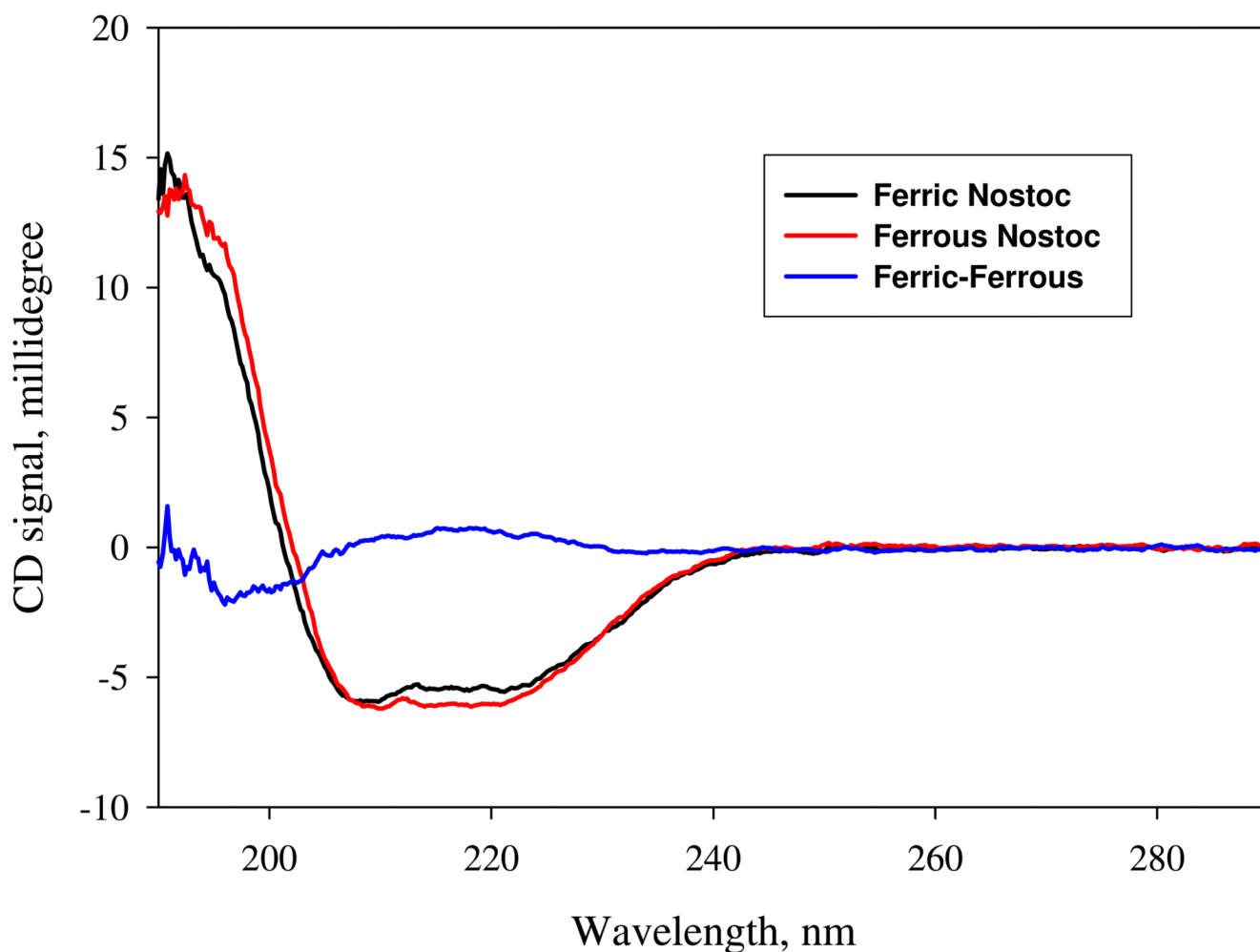
Figure 11.
Far-UV CD of the ferric and ferrous *Ns* H-NOX. Both the ferrous and ferric sensor proteins were prepared as 1 µM in 2 mM HEPES containing 2 mM NaCl and 0.1 % glycerol, pH 7.7 by either dithionite or ferricyanide pre-treatment, respectively, and then gel-filtered in the same HEPES buffer to remove excess reductant or oxidant. CD measurements were conducted as described in the Experimental Procedures. The data shown for the ferric (black), ferrous (red) sensor are 12-scan average corrected for background signal originated from buffer alone and the difference spectrum (blue) is obtained by subtracting the CD spectrum of the ferrous sensor from that of the ferric form.
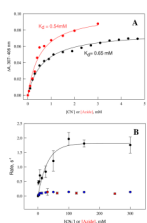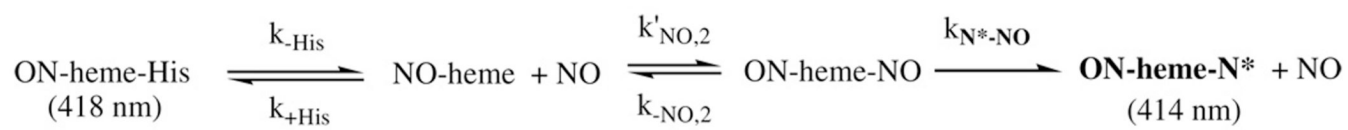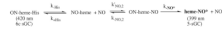
Figure 12.
Equilibrium and kinetic binding of cyanide and azide to the ferric *Ns* H-NOX. To build
binding isotherm for cyanide and azide binding (A), 2.9 µM ferric *Ns* H-NOX was titrated
by aliquots of 0.2 M cyanide to the final concentration of 5 mM (black circles); and 5.8 µM
ferric sensor protein was titrated with 1M azide to 3 mM final concentration (red circles),
respectively, to reach saturation. Maximal absorbance changes at 307 – 406 nm for cyanide
heme complex formation and 377 – 417 nm for azide heme complex formation at different
ligand concentrations were fit by single binding site saturation hyperbola (equation 1) (solid
lines). The volume change by addition of either ligand was less than 2.5% and was not
corrected further for calculating the free ligand concentrations. For kinetic binding
measurements (**B**), 2.9 µM ferric *Ns* H-NOX was mixed with a series of ligand
concentrations at least 10 fold excess to the protein and the absorbance changes at 430 nm in
a stopped-flow. The observed rates obtained by single (for azide, red circles) and double (for
cyanide, black and blue circles) exponential function were plotted against ligand
concentrations. Solid line is the fit to hyperbolic function to show [CN⁻]- dependent
saturation represented by equation 1. Error bars are the standard deviation of triplicate shots.
Reaction temperature for both equilibrium and kinetic binding experiments was 24 °C.

$$\text{ON-heme-His} \underset{k_{+His}}{\overset{k_{-His}}{\rightleftharpoons}} \text{NO-heme} + \text{NO} \underset{k_{-NO,2}}{\overset{k'_{NO,2}}{\rightleftharpoons}} \text{ON-heme-NO} \xrightarrow{k_{N*-NO}} \textbf{ON-heme-N*} + \text{NO}$$

ON-heme-His (418 nm) ... ON-heme-N* (414 nm)

Scheme I.

$$\text{ON-heme-His} \underset{k_{obs_2}}{\overset{k_{obs_1}}{\rightleftharpoons}} \text{NO-heme} + \text{NO} \underset{k_{-on2}}{\overset{k_{on2}}{\rightleftharpoons}} \text{ON-heme-NO} \xrightarrow{k_{off}} \text{heme-NO}^+ + \text{NO}$$

Scheme II.

Table 1

Ligand binding parameter values for the ferrous and ferric sGC and *Ns* H-NOX.

	K_D (M)	k_{OFF}, (s^{-1})	k_{ON}, (M^{-1}s^{-1})	Comments[b]
sGC				
CO	2.6×10^{-4}	10.7	4×10^4	4 °C
NO	4.2×10^{-12} [a]	6×10^{-4}	1.4×10^8	6c (on)/5c (off), 10 °C
O$_2$	N/A	N/A	N/A	No O$_2$ binding at 1 atm, 10 °C
CN$^-$	0.92×10^{-3}	7.2×10^{-5}	7.8×10^{-2}	10 °C
N$_3^-$	2.6×10^{-2}	N/D	N/D	10 °C
_NS_ H-NOX				
CO	1.4×10^{-6}	3.6	3×10^6	6c-CO complex
NO	1.7×10^{-10}	0.05	3×10^8	1st 6c-NO complex
	0.8×10^{-6}	1.9	2.4×10^6	2nd 6c-NO complex
O$_2$	N/A	N/A	N/A	Auto-oxidation
CN$^-$	6.5×10^{-4}	N/A	0.03[c]	[CN$^-$]-dependent saturation[d]
N$_3$	5.4×10^{-4}	N/A	N/A	Limited by Met dissociation

[a] calculated as k_{OFF}/k_{ON} using values from ref. (29,50), N/A - not applicable, N/D - not determined.

[b] Unless otherwise specified, the experimental temperature was 20 – 25 °C.

[c] The dissociation constant for the 2nd step, k_{-2}.

[d] Biphasic kinetics.